GROWTH AND CHARACTERIZATION OF BORON NITRIDE THIN FILMS AND NANOSTRUCTURES USING ATOMIC LAYER DEPOSITION

A THESIS
SUBMITTED TO MATERIALS SCIENCE AND NANOTECHNOLOGY PROGRAM
OF THE GRADUATE SCHOOL OF ENGINEERING AND SCIENCE
OF BILKENT UNIVERSITY
IN PARTIAL FULFILLMENT OF THE REQUIREMENTS
FOR THE DEGREE OF
MASTER OF SCIENCE

By
Ali Haider
August, 2014

I certify that I have read this thesis and that in my opinion it is fully adequate, in scope and in quality, as a thesis for the degree of Master of Science.

_____

Assist. Prof. Dr. Necmi Bıyıklı (Supervisor)

I certify that I have read this thesis and that in my opinion it is fully adequate, in scope and in quality, as a thesis for the degree of Master of Science.

_____

Assist. Prof. Ferdi Karadaş

I certify that I have read this thesis and that in my opinion it is fully adequate, in scope and in quality, as a thesis for the degree of Master of Science.

_____

Assoc. Prof. Tamer Uyar

Approved for the Graduate School of Engineering and Science:

_____

Prof. Dr. Levent Onural

Director of Graduate School

ABSTRACT

GROWTH AND CHARACTERIZATION OF BORON NITRIDE THIN FILMS AND NANOSTRUCTURES USING ATOMIC LAYER DEPOSITION

Ali Haider

M.S. in Materials Science and Nanotechnology

Supervisor: Assist. Prof. Dr. Necmi Biyikli

August, 2014

Being a member of III-nitride family, boron nitride (BN) and its nanostructures have recently attracted a lot of attention, mainly due to their distinctive and superior material properties, including wide band gap, high-temperature stability, high oxidation and corrosion resistance, as well as high thermal conductivity. This versatile material has found applications in UV emission, lubrication, composite reinforcement, gas adsorption, cosmetics, and thermal management. For modern electronic applications, it is imperative to obtain high quality BN films on large area substrates with a controlled thickness in order to fulfill the entire spectrum of hBN applications. Also, a facile method such as atomic layer deposition (ALD) using non halide precursors is necessary to obtain BN films at low temperatures compliant with the standards in terms of having nontoxic byproducts. ALD is a special case of chemical vapor deposition (CVD), in which two or more precursors are sequentially exposed to substrate surface separated by purging periods. In comparison with other thin film growth methods, hall mark of ALD is self limiting growth mechanism which enables deposition of highly uniform and conformal thin films with sub-angstrom thickness control. The precise and conformal layer by layer growth of ALD can be exploited to achieve growth of BN hollow nanofibers (HNFs) on high aspect ratio electrospun polymer nanofibrous templates. BN HNFs fabricated by combination of ALD and electrospinning can be utilized to address and solve important constraints associated with previous methods of fabrication such as

severe preparation conditions, limited control over morphology, and low purity of the resulting BN HNFs.

In this thesis, we report on the controlled deposition of BN films and its nanostructures with the use of a hollow-cathode plasma source integrated (HCPA-ALD) reactor and present detailed materials characterization results of deposited thin films and fabricated nanostructures. Depositions are carried out at low substrate temperatures (less than 450 °C) using sequential injection of non-halide triethylboron (TEB) and N_2/H_2 plasma as boron and nitrogen precursors, respectively. The deposition process parameters such as pulse length of TEB and substrate temperature, as well as the influence of post-deposition annealing are studied. Moreover, another nonhalide alternative precursor named tris(dimethyl)amidoboron (TDMAB) was studied for deposition of BN films. Initial experiments were performed using TDMAB and N_2/H_2 plasma as boron and nitrogen precursor. In addition to BN thin film growth studies, we report on electrospun polymeric nanofibrous template-based fabrication and characterization of AlN/BN bishell HNFs. Synthesized AlN/BN bishell HNFs were found to be polycrystalline with a hexagonal structure along with low-impurity content.

Keywords: Plasma-Enhanced Atomic Layer Deposition, Chemical Vapor Deposition, Boron Nitride, Thin Film, Nanofiber

ÖZET

BOR NİTRÜR İNCE FİLMLERİN VE NANOYAPILARIN ATOMİK KATMAN BİRİKTİRME YÖNTEMİ İLE BÜYÜTÜLMESİ VE KARAKTERİZASYONU

Ali Haider

Malzeme Bilimi ve Nanoteknoloji, Yüksek Lisans

Tez Yöneticisi: Yrd. Doç. Dr. Necmi Bıyıklı

Ağustos, 2014

III-nitrür ailesinin bir üyesi olarak, bor nitrür (BN) ve nanoyapıları geniş bant aralığı, yüksek-sıcaklık kararlılığı, ve yüksek oksitlenme ve korozyon direncinin yanısıra yüksek ısıl iletkenliği de içeren ayırt edici ve üstün malzeme özellikleri sayesinde yakın zamanda çokça dikkat çekmiştir. Bu çok yönlü malzeme UV emisyonu, yağlama, kompozit güçlendirme, gaz adsorpsiyonu, kozmetik, ve ısıl yönetimde uygulamalar bulmuştur. Modern elektronik uygulamalar için, hBN uygulamalarının tüm spektrumunu gerçekleştirmek amacı ile yüksek kaliteli ve kontrollü kalınlığa sahip BN filmlerin yüksek alanlı alttaşlar üzerine elde edilmesi gerekmektedir. Ayrıca, zehirli olmayan yan ürünler elde etmek açısından standartlarla uyumlu şekide düşük sıcaklıklarda BN filmler elde etmek için halojenür içermeyen öncü maddelerin kullanıldığı atomik katman biriktirme (AKB) gibi kolay bir metoda gerek duyulmaktadır. AKB iki ya da daha fazla öncü maddenin arındırma periyotları ile ayrılmış ardışık atımlarla alttaş yüzeyine gönderildiği özel bir kimyasal buhar biriktirme çeşididir. Diğer ince film büyütme metodları ile karşılaştırıldığında, AKB yönteminin ayırt edici özelliği muntazam ve konformal ince filmlerin angstrom-altı kalınlık kontrolü ile biriktirilmesine olanak sağlayan kendi kendini sınırlayan büyütme mekanizmasıdır. AKB yönteminin kesin ve konformal katman katman büyütme tarzı elektro lif çekimi yöntemi ile elde edilmiş yüksek boy/en oranına sahip polimer nanolif şablonlar üzerine BN oyuk nanoliflerin büyütülmesini

gerçekleştirmek amacıyla da kullanılabilir. AKB ve elektro lif çekimi yöntemlerinin birlikte kullanılmasıyla üretilen BN oyuk nanolifler, ağır hazırlama koşulları, morfoloji üzerindeki sınırlı kontrol, ve elde edilen BN oyuk nanoliflerin düşük saflığı gibi, önceki üretim metodları ile ilgili önemli kısıtlamaları tanımlamak ve çözmek amacıyla kullanılabilir.

Bu tezde, BN filmlerin ve nanoyapıların oyuk katod plazma (OKP) kaynağı entegre edilmiş bir reaktörün kullanımıyla kontrollü bir şekilde büyütülmesini rapor etmekte, biriktirilen ince filmler ve üretilen nanoyapılar için detaylı malzeme karakterizasyon sonuçları sunmaktayız. Biriktirmeler düşük alttaş sıcaklıklarında (450 °C'den düşük), boron ve nitrojen öncü maddelerinin, sırasıyla halojenür olmayan trietilbor (TEB) ve N_2/H_2 plazmanın ardışık enjeksiyonu kullanılarak gerçekleştirilmiştir. TEB'un atım süresi ve alttaş sıcaklığı gibi biriktirme süreç parametrelerinin yanısıra biriktirme sonrası tavlamanın etkileri de incelenmiştir. Ayrıca, BN filmlerin biriktirilmesi için tris(dimetil)amidobor (TDMAB) isimli, halojenür içermeyen diğer bir alternatif öncü madde araştırılmıştır. İlk deneyler, bor ve nitrojen öncü maddeleri olarak TDMAB ve N_2/H_2 plazmanın kullanılmasıyla gerçekleştirilmiştir. BN ince film büyütme çalışmalarına ek olarak, AlN/BN iki kabuklu oyuk nanoliflerin elektro lif çekimi yöntemi ile elde edilmiş polimerik nanolif şablon-temelli üretimini ve karakterizasyonunu rapor etmekteyiz. Sentezlenen AlN/BN iki kabuklu oyuk nanoliflerin düşük safsızlık içeriği ile birlikte hegzagonal yapıya sahip ve çok taneli olduğu bulunmuştur.

Anahtar Kelimeler: Plazma-Destekli Atomik Katman Biriktirme, Kimyasal Buhar Biriktirme, Bor Nitrür, İnce Film, Nanolif

Acknowledgement

I would like to thank my supervisor, Prof. Dr. Necmi Biyikli, for the guidance, encouragement and advice he has provided throughout my time as his student. I want to express my gratitude to Cagla Ozgit-Akgun and Eda Cetinorgu-Goldenberg, for their continued support, help, and encouragement. I would also like to thank all engineers especially Semih Yasar, Mustafa Guler, and Enver Kahveci who contributed to my research experience and always helped me in enhancing my learning towards research equipments. Finally, I want to acknowledge Higher Education Commission of Pakistan (HEC) for Human resource development (HRD) fellowship for MS leading to PhD.

Contents

List of Figures

List of Tables

Chapter 1

Introduction

1.1 Historical Background

Atomic layer deposition (ALD) is a special case of chemical vapor deposition technique where thin film deposition is achieved by dividing the reaction into two half cycles by sequential exposure of precursors separated with purge/evacuation periods. Hall marks of ALD are excellent surface coverage, highly conformal films, and precise thickness control at atomic scale owing to self-limiting reactions of precursors occurring at the substrate surface.

The origin of ALD dates back to 1970s. The credit of first realizing the principles of ALD is given to two different groups. The more acknowledged pioneer of ALD is Tuomo Suntola, who demonstrated ALD under the name of atomic layer epitaxy (ALE). The beginning of ALD dates back to a patent published in 1970s in which following processes were demonstrated: growth of ZnS by Zn/S precursors, growth of SnO_2 by Sn/O_2 precursors, and growth of GaP by Ga/P precursors. The first commercial application of ALD has been demonstrated in manufacturing of thin film electroluminescent displays in 1980s [1].

On the other hand, less acknowledged pioneer of ALD is a research group in Soviet Union headed by Professor Aleskovskii. Shevjakov et al. first described the $TiCl_4/H_2O$ process to grow layers of TiO_2 and $GeCl_4/H_2O$ process to grow layers of GeO_2 in the proceedings of a conference, which was organized in 1965, and published in 1967. The Soviet Union researchers defined this technique as "molecular layering" [2].

Partly because of its history, and partly because of its unique properties, this technique has been referred with many different names. The current most widely used name is ALD, which dates back to early 1990s [3]. Plasma-enhanced ALE was first demonstrated in 1991 by De Keijser and Van Opdorp from Philips research laboratories in Eindhoven, Netherlands [4]. In their study, remote microwave-induced plasma was utilized to generate hydrogen radicals which were subsequently used for the growth of gallium arsenide. A major driving force for ALD is in the prospective seen in continuous scaling down of microelectronic devices by using ALD. Table 1.1 represents the alternative names and abbreviations of ALD which have been used in history instead of ALD.

Table 1.1: Alternative names of ALD[5]

Name	Abbreviation
Atomic layer chemical vapor deposition	ALCVD
Atomic layer deposition	ALD
Atomic layer epitaxy	ALE
Atomic layer evaporation	ALE
Atomic layer growth	ALG
Chemical assembly	
Digital layer epitaxy	DLE
Molecular deposition	
Molecular lamination	
Molecular layer epitaxy	MLE
Molecular layering	ML

1.2 An Overview on Atomic Layer Deposition

ALD is a special type of CVD technique, in which unlike CVD, one reaction is splitted into two half reactions by exposing the reactants alternatively to the substrate surface, separated by an inert gas purge. As there are only limited number of reaction sites on the substrate after exposure of one precursor, one growth cycle will only deposit a fraction of a monolayer (sub-monolayer) of species. If both half reactions will be self-limiting, the growth will continue in a sequential manner to deposit a thin film with highly precise atomic-scale thickness control. This unique self terminating film growth mechanism also brings other advantages such as high conformality and high uniformity of the grown films [6].

1.2.1 Mechanism

Figure 2.1 shows a schematic representation of a typical ALD cycle. Layer by layer material growth consists of following four steps:

(1) Exposure of first precursor, precursor adsorbs on reactive sites and reaction products are formed.

(2) Purge to evacuate the reactor from unreacted excess precursor molecules and gaseous reaction by-products.

(3) Exposure of second precursor, which reacts with the adsorbate to form a monolayer of desired material.

(4) Purge to remove unreacted material and byproducts of the reaction.

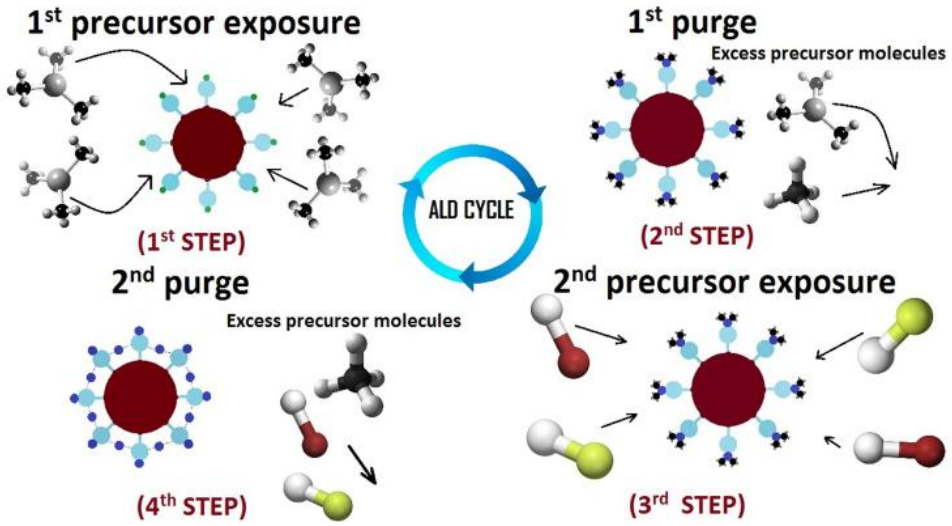

Figure 1.1: Schematic representation of an ALD cycle consisting of four steps.

As precursor molecules are exposed separately, each ALD cycle results in a monomolecular layer of the given precursor, which eventually becomes independent of the precursor exposure after saturation of the reactive surface sites. Therefore, ALD has the advantage of layer-by-layer self-limiting and ultimate conformal growth on high aspect ratio structures. After the completion of one cycle, substrate surface is returned back to its original state and is ready for the next cycle. As the amount of material deposited in one cycle remains constant after complete initial nucleation of the film, a film with desired thickness can simply be achieved by repeating the reaction cycles.

Three types of chemisorption reactions contribute to self-limiting reactions of ALD via compound reactants [5,7]:

1.2.1.1 Ligand Exchange

$$II - a + ML_{z(g)} \rightarrow II - ML_{z-1} + aL_{(g)} \qquad (1.1)$$

Ligand exchange mechanism refers to splitting of a reactant molecule (ML_z), followed by ligand (L) association with surface group (II-a). It can also occur

between the surface group and adsorbed ML_{z-y} complex. A volatile compound (aL) is the reaction byproduct of ligands exchange reaction.

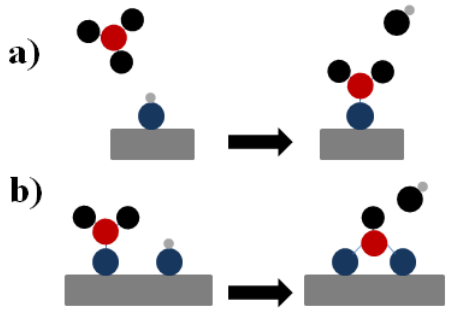

Figure 1.2: (a) Ligand exchange reaction of the ML_z reactant with surface "-*a*", releasing gaseous byproduct *a*L. (b) Ligand exchange can also occur between the surface group and adsorbed ML_{z-y} complex.

1.2.1.2 Dissociation

$$IIM' - ZII + ML_{z(g)} \rightarrow IIM' - L + IIZ - ML_{z-1} \qquad (1.2)$$

Dissociation mechanism refers to dissociation of reactant on reactive M-Z sites on the surface. After the reactive sites are taken up by the reactant molecule, surface is called saturated and reaction is self terminated. Dissociation may continue on the surface; but it does not affect the number of bonded M atoms and the number of bonded ligands.

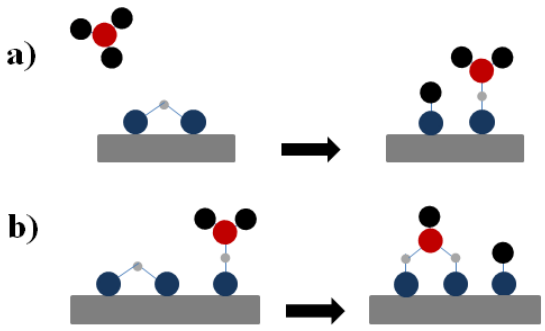

Figure 1.3: (a) Dissociation of the ML_z in surface M-Z sites. (b) Dissociation may also occur between MZ_{z-y} complex and M-Z sites.

1.2.1.3 Association

$$II + ML_{z(g)} \rightarrow II...ML_z \qquad (1.3)$$

In association mechanism, adhering of reactant occur to reactive sites without releasing the legends. A coordinative bond is formed with the reactive surface sites.

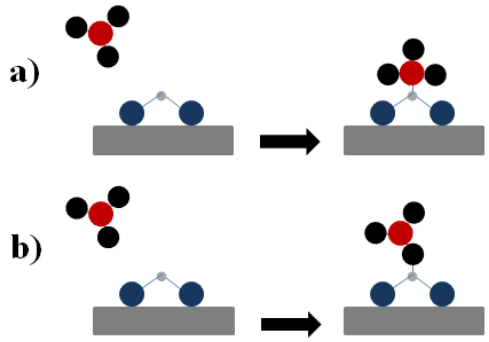

Figure 1.4: Association of the ML_z complex onto the surface. (a) Association can occur through formation of a coordinative bond between the central M ion and the surface, (b) or perhaps between the ligands and the surface.

1.2.2 Factors Causing Saturation and Growth of Less than Monolayer per Cycle

After one cycle is completed, a certain amount of material is deposited on the substrate surface called growth per cycle (GPC). Although there is a common misconception that one ALD cycle deposits one monolayer of material, the reality is different. GPC value is often less than a monolayer per cycle due to the effect known as "steric hindrance". Highest GPC value correspond to completion of reaction by maxium number of surface sites reacting with the reactant through legend exchange. Usually a limited number of reactive sites are occupied by the reactants and steric hindrance terminates it [8,9]. The bulky legends block the remaining bonding sites and therefore the surface can be considered as full due to steric hindrance. The other reason of sub-monolayer saturation is the limited number of reactive sites in which the number of bonding sites is less than required to achieve a full ligand coverage [10,11].

1.2.3 Effect of Number of Cycles on GPC

The first ALD cycle exposes the reactants on the original substrate material, and the following cycles occur on the substrate already exposed to the reactants in previous cycle. Finally after some successive initial growth cycles, when surface of the substrate is totally covered with the ALD grown material, reactants are only exposed to the ALD grown material. With the change in chemical composition of the surface, GPC generally varies with the number of cycles within the initial phase of deposition.

GPC variation with the number of ALD cycles can be classified into four general cases. GPC saturates to a constant value after a certain number of ALD cycles in all of the four cases. In linear growth [Fig. 2.5(a)], GPC is constant starting from the first cycle [12,13]. Linear growth can take place when number of reactive sites does not change with the number of growth cycles and steric hindrance from the bulky legends cause the saturation. The second case is substrate enhanced growth [Fig. 2.5(b)], in which GPC is higher during the early growth phase and slowly decrease as the ALD cycles proceed on the substrate surface [14,15]. Initial higher GPC is referred to non-constant growth in transient regime. Substrate enhanced growth takes place when number of reactive sites on the original substrate is higher than the number of reactive sites on ALD grown material.

The third case is called substrate inhibited growth [Fig. 2.5(c)], in which GPC is lower in the early growth cycles and becomes constant in the steady state regime after nucleation has completed [16,17]. This type of growth is caused by lower number of reactive sites at the substrate then on the ALD deposited material.

In the fourth case [Fig. 2.5(d)], GPC is lower during initial growth cycles and it goes through a maxima before reaching to steady state value of GPC [18].

Initial low growth is caused by the lower number of reactive sites at the substrate then on the ALD deposited material and a maxima is caused due to island growth (three-dimensional growth mode) of deposited material.

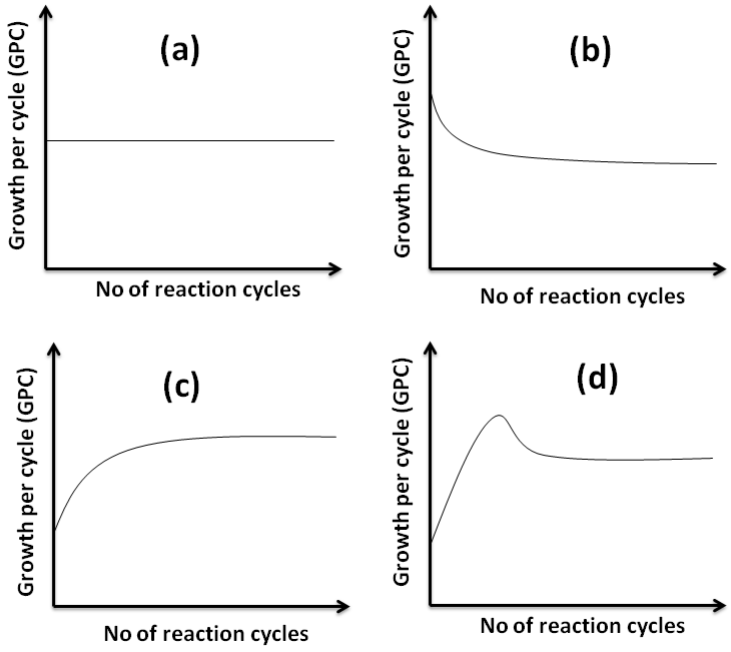

Figure 1.5: Dependency of the GPC on the number of reaction cycles in different types of ALD processes: (a) linear growth, (b) substrate-enhanced growth, (c) substrate-inhibited growth of Type 1, and (d) substrate-inhibited growth of Type 2.

1.2.4 Effect of Temperature on GPC

Variation of GPC with temperature arise from the influence of temperature on the number and type of reaction sites present as well as the effect of temperature on the preferred reaction mechanism. There are four characteristic cases in which GPC might depend on the temperature range where ALD process satisfies the self-limiting reaction condition.

1. The GPC may decrease with temperature when the number and type of reactive sites is the dominant mechanism to control the amount of chemisorbed species [Fig. 2.6(a)] and the number of reactive sites

decreases with temperature. Increasing the temperature may also change the chemisorption mechanism [19,20].

2. GPC stays constant with increasing temperature in the case where steric hindrance causes growth saturation [Fig. 2.6(b)] and there is no or very little effect of temperature on reactive sites [21].
3. GPC may increase with temperature [Fig. 2.6(c)]. In that case, some energy barriers are crossed at higher temperature and some reactions may become active which were not active initially at low temperatures [22,23].
4. GPC may first increase and then decrease with temperature [Fig. 2.6(d)]. In that case, some reactions are activated initially with increase in temperature but at higher temperature, number of reactive sites begin to decrease which inturn decreases GPC [24,25].

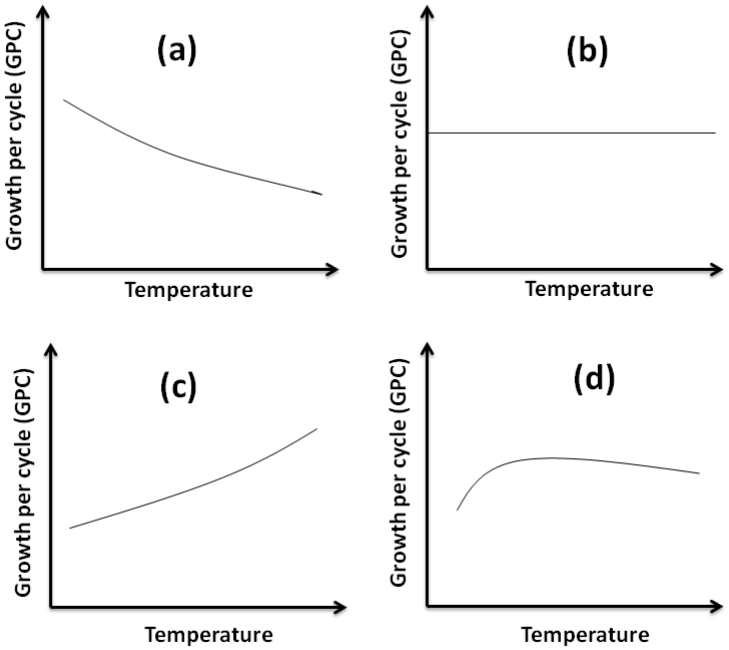

Figure 1.6: Variation of the GPC with the ALD processing temperature in the ALD window: (a) the GPC decreases with temperature, (b) the GPC is constant with temperature, (c) the GPC increases with temperature, and (d) the GPC first increases and then decreases with temperature.

1.2.5 Growth Modes of ALD

The material arranges itself on the surface in specific manners during ALD growth which is known as the growth mode. Multilayer adsorption should be excluded by definition in ALD growth mode of monolayer per cycle due to self-limiting nature of ALD. In ideal two dimensional layer-by-layer growth mode [Fig. 2.7(a)], material is being deposited in the lowest unfilled material layer as one monolayer of ALD grown material which covers the substrate completely [26,27]. In island growth mode, new units of materials are preferentially deposited on already deposited material by ALD [Fig. 2.7(b)]. Several ALD processes follow this type of growth model [28,29]. Another model named random deposition model is a growth mode in which new material units are deposited on all the surfaces with an equal probability [Fig. 2.7(c)] [30]. The growth mode may also change during growth, as for example it may be two dimensional for the initial monolayer and then island or random growth may prevail [31].

Only few of the experimental investigations published so far have found the relationship between growth modes and way in which GPC varies with the number of cycles. It has been found that surface inhibited growth follows the island growth mode [32,33] and linear growth follows two dimensional [34] and random growth mode [35].

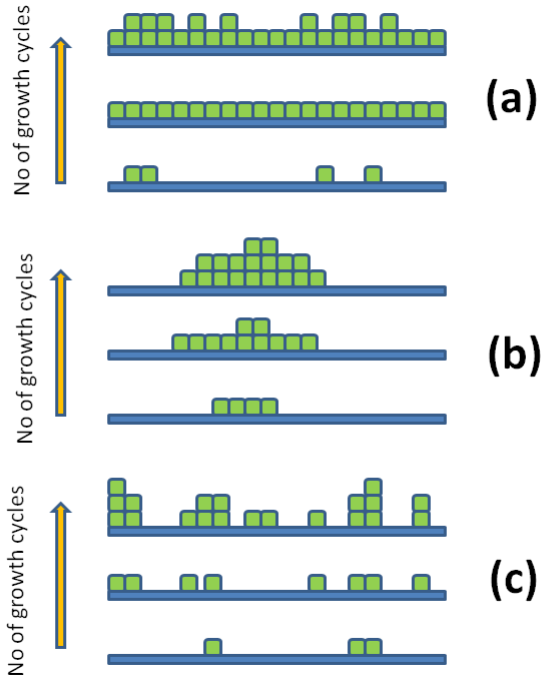

Figure 1.7: Schematic illustration with increasing number of growth cycles of selected growth modes possible in ALD: (a) two-dimensional growth, (b) island growth, and (c) random deposition.

1.2.6 ALD Window

ALD window is the temperature range in which self-limiting growth occurs. In this temperature range, deposition has an ideal constant growth rate with deposition of one monolayer per cycle. Center line (Fig. 2.8) indicates the ALD window on the growth rate vs. temperature graph. Deviation from ideal self limiting ALD line corresponds to different mechanisms which prevent ALD to attain the requirement of self-limiting reactions. Below the ALD window, there are two possible mechanisms which contribute to non-self terminating reactions. One belongs to high deposition rate due to condensation of precursor molecules on substrate surface at low temperatures. Other belongs to very low deposition rates at low temperatures which is possible due to incomplete reactions due to slower mass transport and low reaction rates. On the other hand, at high temperatures, thermal decomposition occurs which causes a CVD-like growth

mechanism in which gas phase decomposition of precursor molecules occurs. In addition, deposition rate may decline at higher temperatures due to desorption of monolayer's deposited by ALD [5].

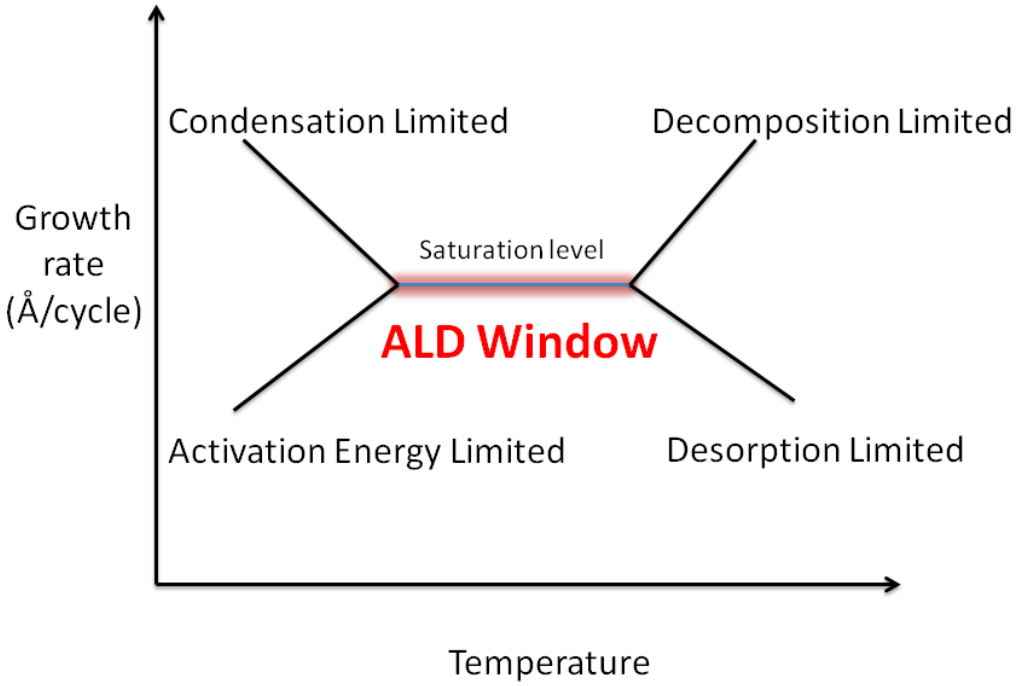

Figure 1.8: Effect of deposition temperature on the ALD growth rate.

1.2.7 Merits and Demerits of ALD and Comparison with Other Deposition Techniques

Table 1.2: Merits and demerits of ALD

Merits	Demerits
Simple and accurate thickness control by changing the number of reaction cycles	Slow growth rate
Excellent conformality and uniformity	Low precursor utilization efficiency
Atomic level control of material composition	
High quality material deposition at low processing temperatures	
No need of reactant flux homogeneity, which enables large area and batch capability	
Good reproducibility and straight forward scale-up	
No gas phase reactions occur, favoring the usage of precursors that are highly reactive towards each other	
Capability to prepare multilayer structures in a continuous process	

Table 1.3: Comparison of ALD with other thin film deposition techniques [36].

Method	ALD	CVD	MBE	Sputter.	Evapor.	PLD
Thickness Uniformity	Good	Good	Fair	Good	Fair	Fair
Film Density	Good	Good	Good	Good	Good	Good
Step Coverage	Good	Varies	Poor	Poor	Poor	Poor
Interface Quality	Good	Varies	Good	Poor	Fair	Varies
Low Temp. Deposition	Good	Varies	Good	Good	Good	Good
Deposition Rate	Poor	Good	Fair	Good	Good	Good
Lack of Pinholes	Good	Good	Good	Fair	Fair	Fair
Automated Multilayers	Good	Fair	Good	Good	Fair	Fair
Industrial Applicability	Varies	Good	Varies	Good	Good	Poor

MBE= Molecular beam epitaxy, CVD= Chemical vapour deposition, and PLD- Pulsed laser deposition

1.2.8 Classes of Precursors Utilized in ALD

One of the most primary requirements for reactants/precursors that can be utilized in ALD is that they must be volatile and must not thermally decompose in the ALD window (ALD processing temperature where condition of self terminating reaction is satisfied). Other requirements include complete reactions with no etching of the film or the substrate, volatile but inert/non-etching byproducts, and sufficiently high purity. Other common CVD precursor requirements apply as well, such as reasonable cost, easy synthesis and handling, and environmental compatibility [37]. Generally, reactants used in ALD process can be divided in two main categories: inorganic reactants and metal organic reactants.

Metal organic reactants can be further classified in to two sub groups in which one of them contains a direct metal carbon bond and other one contains no direct metal carbon bond. In the group of inorganic reactants most common reactants are halides and elements. While in the group of organometallic reactants, alkyls and cyclopentadienyls are common. Other subclasses of organometallic reactants include alkoxides, diketonates, amides, and amidinates. Elements are the most simple type of reactants used in ALD. They seem very attractive as they carry no extra ligands which can potentially solve the problem of steric hindrance. However, low vapor pressure of elements and their reversible adsorption are the key aspects which limits their usage in ALD processes. Halides are the second class of inorganic precursors which are highly reactive and thermally very stable. In addition to high reactivity, small size of their ligands is very attractive to minimize steric hindrance effect. However, one of the key limitation of halides is their acidic byproducts which are corrosive and can etch the film or reactor components. Alkyls are true organometallic compounds which contain direct metal to carbon bond. These kind of reactants are reactive and their ligands size is also small which helps in reducing the steric hindrance effect. The disadvantage of alkyls is their low decomposition

temperature. In this thesis, TEB is used as metal precursor for growth of BN thin film and nanostructures which is an alkyl precursor and contains direct metal to carbon bond. The common non-metal precursors used in ALD processes are: water (H_2O), oxygen (O_2), ozone (O_3), alcohols (R-OH), hydrogen peroxide (H_2O_2), atomic oxygen created from plasma as the O_2, ammonia (NH_3) or nitrogen/ammonia (N_2/NH_3) plasma [38,39].

1.2.9 Plasma vs. Thermal ALD

Exchange reactions between precursor molecules and surface species can be enhanced by providing an external source of activation energy. In the conventional mode of ALD, called thermal ALD, activation energy is provided thermally by heating the entire reactor chamber or the substrate. One alternative of thermal ALD is plasma-enhanced ALD (PEALD) (also called as plasma-assisted ALD, PA-ALD), in which plasma is utilized to create high energy ions and radicals which enhance the surface reactions by providing an additional source of activation energy.

PEALD open the door for the usage of temperature sensitive substrates in ALD by lowering the deposition temperature. Also, with the use of PEALD, reactants which decompose at higher temperatures can be utilized for surface reactions of ALD. PEALD enables shorter deposition times (higher growth rates), which increase the throughput and make it more attractive for mass production. The main drawback or limitation of PEALD process is reduced conformality on high aspect ratio structures, which is due to the recombination of radicals in deep trenches of high aspect ratio nanostructures.

In comparison with thermal ALD, the PEALD chamber configuration is more complicated. There are three main reactor configurations for PEALD depending on the position of the plasma source, namely, radical-enhanced, direct, and remote plasma systems (Figure 2.9). The first ALD reactor

configuration is radical-enhanced ALD which is a modified version of thermal ALD with the addition of a plasma generator [Fig 2.9(a)]. Plasma generation takes place relatively far distance from substrate surface. Therefore, ions and radicals recombine before reaching the substrate. Radicals with low surface recombination probability are needed in this type of configuration in order to increase the efficiency.

In direct plasma configuration [Figure 2.9(b)], a capacitive-coupled plasma is generated at radio frequency (RF, 13.56 MHz) between two parallel electrodes in which one of them is powered while the other one is grounded. Fluxes of plasma radicals and ions are very high in this configuration since plasma is generated very close to substrate surface. As a result, even short exposure times provide uniform deposition on larger wafer surfaces. Processing conditions must be optimized carefully for the sake of avoiding plasma damage from emission of high energy photons.

Remote plasma ALD [Figure 2.9(c)] refers to generation of plasma source at a remote location from substrate holder. The main advantage of this configuration is the high flux of radicals as compared to radical enhanced ALD due to generation of downstream plasma. In addition, this configuration provides better control over plasma and substrate conditions which is not possible for direct plasma ALD.

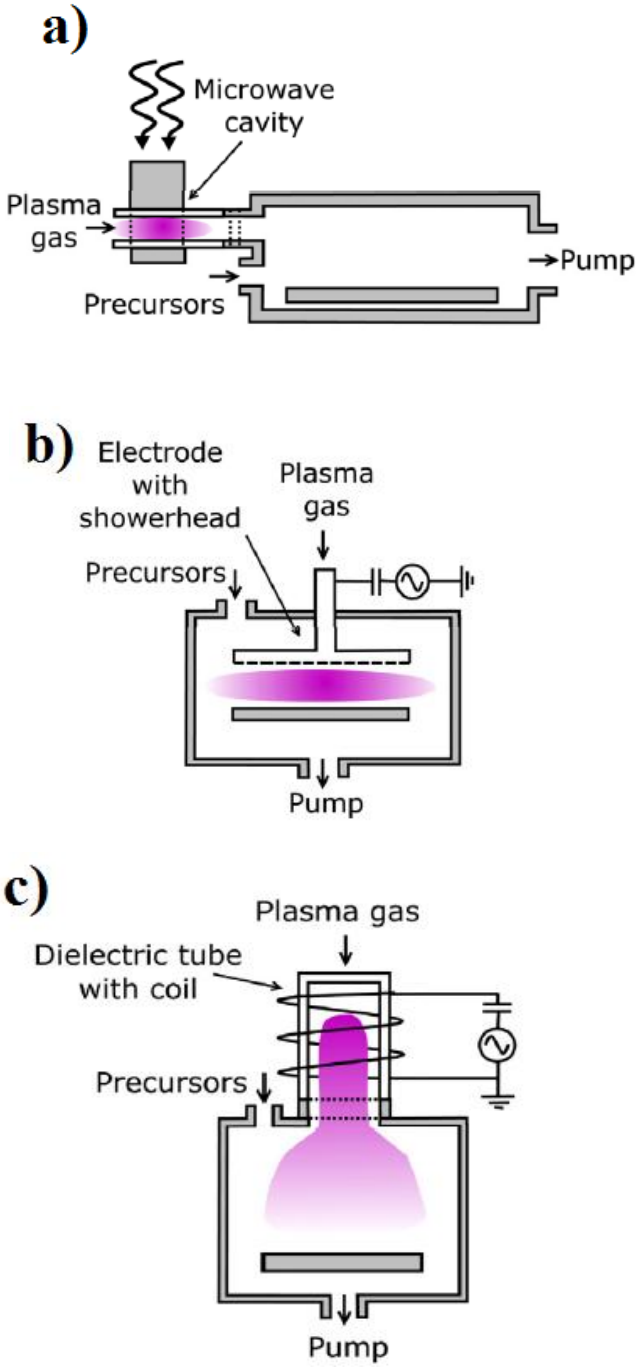

Figure 1.9: Three main types of plasma reactor configurations for PEALD. (a) Radical-enhanced, (b) direct plasma, and (c) remote plasma configurations [40].

The plasma source used in this thesis for deposition of BN thin film and nanostructures is hollow cathode plasma (HCP) source in HCPA-ALD reactor. It has a major advantage over inductively couple and microwave plasma sources

in terms of low oxygen contamination. Oxygen contamination is a major problem with inductively couple and microwave plasma sources that arise due to interaction between the plasma species and ceramic introduction windows. Easy scalability and reduced start up times are the other advantages that HCP possess [41].

1.3 Motivation

Being a member of III-nitride family, boron nitride (BN) and its nanostructures have recently attracted a lot of attention, mainly due to their distinctive and superior material properties, including wide band gap, high-temperature stability, high oxidation and corrosion resistance, as well as high thermal conductivity. This versatile material has found applications in UV emission, lubrication, composite reinforcement, gas adsorption, cosmetics, and thermal management. In order to fulfill the entire spectrum of hBN applications, it is imperative to obtain high quality BN films on large area substrates with precise and uniform thickness control. Moreover, a reliable and relatively facile method is necessary to obtain BN films at low temperatures compliant with the standards in terms of having nontoxic byproducts. The need for high-quality and conformal ultra-thin films on large area substrates together with the development of suitable deposition techniques has increased in recent years. These specific requirements, which cannot be fulfilled using conventional physical vapor deposition (PVD) or chemical vapor deposition (CVD) methods, can be met by ALD. In addition, with the combination of ALD and electrospinning, BN nanostructures can be fabricated which might be utilized to address and solve important constraints associated with previous methods of functional nanostructured materials synthesis, such as severe preparation conditions, limited control over morphology, and low purity of the resulting BN nanotubes.

Unlike other CVD methods, ALD is based on the saturative surface reactions, which results in a self-limiting growth mechanism. As a result, excellent conformality and large-area uniformity in addition to accurately controlled film thickness are inherently obtained. The processing temperatures can also be kept low, which makes ALD attractive and applicable for a wide range of substrates including transparent and flexible polymers.

1.4 Objectives

This thesis mainly focuses on the growth recipe development and material characterization of BN deposited via sequential injection of triethylboron (TEB) and N_2/H_2 plasma using a hollow-cathode plasma source integrated ALD reactor. Nonhalide, alkyl precursors have been utilized for the first time to achieve controlled deposition of BN. In addition, tris–dimethylamino borane (TDMAB) has been used as an alternative precursor for the low-temperature deposition of BN. The main aim of the work is to obtain high-quality, conformal, and uniform deposition of BN films on large area substrates using hollow cathode plasma-assisted ALD (HCPA-ALD) at low substrate temperatures with a systematic optimization of growth parameters such as pulse length of precursors and substrate temperature.

Another goal of this work was to demonstrate the effectiveness of the ALD method to fabricate ceramic nanostructures. To achieve this goal, AlN/BN HNFs were fabricated using a template-based method, which combines the electrospinning, ALD, and CVD processes sequentially. As a proof of concept study, we report on structural, morphological and compositional properties of AlN/BN bishell HNFs fabricated via successive combination of HCPA-ALD and sequential plasma-assisted CVD on electrospun polymeric nanofibrous templates.

1.5 Literature overview

1.5.1 BN Thin Film Deposition Using HCPA-ALD Reactor

BN and carbon are isoelectronic and isostructural analogues of each other. Similar to carbon materials, BN can exist in the form of different phases such as amorphous (aBN), turbostratic (tBN), hexagonal (hBN), and cubic (cBN). Among the known two-dimensional materials, hBN and graphene are isostructural, yet their physicochemical properties are different. Graphene is the most prominent member of family of layered materials while hBN is an inorganic analog of graphene. hBN structure consists of layers of hexagonal sheets, which establishes it as an insulator with a direct band gap of ~5.9 eV in its single crystal form [42,44]. Boron and nitrogen atoms are bonded together with a strong covalent bond within each hBN sheet, while different layers of hBN are bound by Van der Waals forces along the *c*-axis at a distance of 6.66 Å. Different phases of BN have been used as powders and coatings in their pure form or as a composite. This versatile material has found applications in metallization, metal industry, high temperature furnaces, cosmetics, and thermal management. hBN is mainly used for high temperature crucibles and evaporator boats, and as a lubricant due to its layered structure. hBN offers a significant advantage over conventional lubricants due to its high temperature stability and high oxidation resistance [42-49]. The interest in the fabrication of thin films and coatings of either hBN or cBN stems from their high structural strength, high temperature stability, high oxidation resistance, low surface energy, and high thermal conductivity, which already led to numerous technological applications. Application of hBN as a dielectric layer for graphene based electronics has been reported. UV lasing has also been demonstrated with the production of high quality hBN flakes by Kubota et al. Their high quality hBN flakes paved the way to demonstrate applications of hBN in UV light emitting diodes [45,46].

Producing high quality BN thin films has proven to be very challenging. BN films deposited by physical vapor deposition (PVD) suffer from poor adhesion and cracking [50,51], whereas BN films deposited by CVD might result in a mixture of hBN, tBN and cBN phases [52,54]. Boron/nitrogen precursors used to obtain hBN films through CVD are reported as BF_3/NH_3, BCl_3/NH_3, and B_2H_6/NH_3 [55-57]. Post-deposition annealing is routinely utilized for structural enhancement, surface roughness control and intrinsic stress elimination in thin films. Structural ordering of hBN has been accomplished using proper annealing. Researchers have also employed ALD technique for BN thin film deposition to obtain highly conformal and uniform BN films with simple thickness control. BN films obtained via ALD were either aBN or tBN, in which BBr_3/NH_3 and BCl_3/NH_3 were utilized as boron/nitrogen precursors, respectively [58-60]. Substrate temperatures for self-limiting growth was reported to be in the range of 250-750 °C. However, due to the nature of these halide precursors, the byproducts of surface reactions are hazardous and corrosive [61,62]. hBN deposition with borazine, which is a non-halide precursor, has been reported to result in a monolayer limited deposition under ultra high vacuum conditions on transition metal surfaces [63,64]. The deposition terminated or became very slow after the formation of an initial monolayer of BN, therefore deposition was believed to be surface inhibited due to the inert nature of boron nitride.

1.5.2 Fabrication of Aluminium Nitride (AlN)/BN Bishell Hollow Nanofibers (HNFs)

AlN and BN have similar lattice parameters and they are well known for their attractive properties, mainly including large band gap, high temperature stability, high oxidation and corrosion resistance, and high thermal conductivity. Nanostructures of AlN have emerged as a promising candidate for high surface area, highly sensitive biological and chemical sensors [65,66]. Mostly AlN

tubular structures have been synthesized at high temperature using template free methods. Recently our group has reported template based synthesis of AlN at temperatures as low as 200 °C using electrospinning and ALD [67].

BN and boron nitride nanotubes (BNNTs) are structural analogues of carbon and carbon nanotubes (CNTs) respectively. BN exists in the various forms such as rhombohedral (r-BN), hexagonal (h-BN), cubic (c-BN), turbostratic (t-BN) and amorphous (a-BN) [68]. In contrast to metallic or semiconducting CNTs, BNNT has band gap of 5.5 eV, independent of tube chirality and morphology. Primarily, the interest in BN nanotubes arose due to a recognized fact that layered BN structure is much more thermally and chemically stable then graphite carbon structure. Later on, researchers have demonstrated that BNNTs exhibit far better thermal and chemical stabilities than CNNTs. With these inherited properties in BN tubular structures, researchers have shown BNNTs application in composite reinforcement, gas adsorption, membrane filters, field emitters, and ultraviolet light emitters [69].

In the recent years fibrous hollow structures have gathered huge interest of researchers due to their unique characteristics such as large surface area, high aspect ratio, and open pore structures. The pioneering work in BNNTs synthesis was conducted by Chopra et al. [70], followed by some other groups [71,72] who prepared BNNTs by arc discharge method. However carbon impurities were present in those tubes and BN nanoparticles were yielded with BNNTs and observed at BNNTs tip ends. Laser ablation synthesis of BNNTs was reported by Golberg et al. [73], where a continuous CO_2 laser was focused on BN targets at higher temperatures. Limitations associated with this method is the high percentage of BN flakes that were obtained with a rather small number of BNNTs. CVD synthesis of BNNTs have been reported by Lourie et al. [74], at higher temperatures ranging from 700-1100 °C. However, In contrast with hundred of grams CVD yielded CNTs, Researchers have struggled to obtain huge amount of BNNTs with CVD. Instead a milligram product has been obtained containing BNNTs. In this thesis, we report on AlN/BN bishell HNFs fabrication by a combination of electrospinning and HCPA-ALD.

Chapter 2

Experimental Details

This chapter provides a detailed explanation of boron nitride (BN) thin film deposition and fabrication of aluminium nitride (AlN)/BN bishell hollow nanofibers (HNFs) as well as the materials characterization techniques. All of the deposition and fabrication processes were performed at UNAM Cleanroom Facility (UCF) and UNAM characterization tools were used for materials property evaluation of thin film and nanostructured BN materials.

2.1 BN Deposition Using Sequential Injection of Triethylboron (TEB) and N_2/H_2 Plasma

BN thin films were deposited on silicon (Si) (100) wafers. Substrate cleaning procedure started with 5 min sequential ultrasonic agitation in isopropanol, acetone, methanol, and de-ionized (DI) water. Following that, substrates were immersed in (1:25) HF: H_2O mixture for 1 min to remove native oxide on substrate surface. At the end of cleaning procedure, Si (100) wafer pieces were rinsed with DI water and dried using nitrogen (N_2) gun.

Depositions were performed in a modified Fiji F200-LL atomic layer deposition (ALD) reactor (Cambridge Nanotech Inc., Cambridge, MA) which is equipped with a stainless steel hollow cathode plasma source (Meaglow Ltd., Thunder Bay, ON, Canada). The Fiji is a modular high-vacuum ALD system which is capable of carrying out thermal as well as plasma-enhanced depositions. The details of the system are presented in Fig. 3.1.

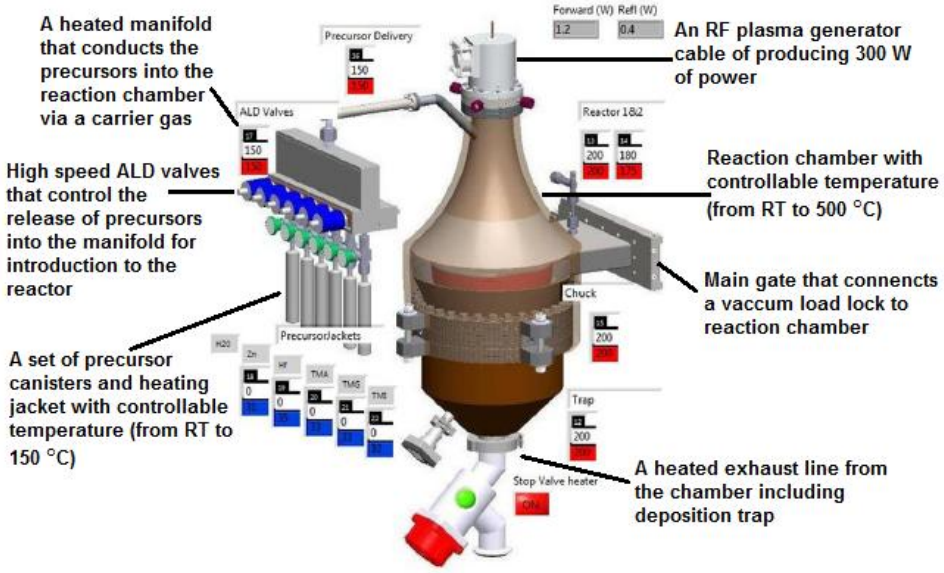

Figure 2.1: Details regarding specific parts and their features of ALD system

BN thin films were deposited on pre-cleaned substrates using sequential exposures of TEB and N_2/H_2 plasma at temperatures ranging from 250 to 450 °C. Due to its relatively low vapor pressure (boiling point = 95 °C), TEB precursor was heated up to 45 °C. The base pressure of the system was kept at 150 mTorr. TEB and N_2/H_2 were carried from separate lines using 30 and 100 sccm Ar, respectively. N_2/H_2 gas flow rates and plasma power were kept constant in all experiment as 50/50 sccm and 300 W, respectively. Ar was used as a purging gas with 10 and 20 s of purge duration.

2.2 BN Deposition using Sequential Injection of Tris(dimethyl)amidoboron (TDMAB) and N_2/H_2 Plasma

BN thin films were deposited on silicon (Si) (100) wafers. Substrate cleaning procedure started with 5 min sequential ultrasonic agitation in isopropanol, acetone, methanol, and de-ionized (DI) water. Following that, substrates were immersed in (1:25) HF: H_2O mixture for 1 min to remove native oxide on substrate surface. At the end of cleaning procedure, Si (100) wafer pieces were rinsed with DI water and dried using nitrogen (N_2) gun.

Depositions were performed in a modified Fiji F200-LL ALD reactor (Cambridge Nanotech Inc., Cambridge, MA) which is equipped with a stainless steel hollow cathode plasma source (Meaglow Ltd., Thunder Bay, ON, Canada). The details of the system are given in Fig. 3.1. BN thin films were deposited on pre-cleaned substrates using sequential exposures of TDMAB and N_2/H_2 plasma at temperatures ranging from 50 to 400 °C. 800 growth cycles were carried out and one hollow cathode plasma-assisted ALD (HCPA-ALD) cycle consisted of 0.06 s TDMAB pulse/10 s Ar purge/40 s N_2/H_2 plasma (50/50 sccm, 300 W)/10 s Ar purge.

2.3 Post-growth Annealing of BN Thin Films

BN deposited on Si substrate by exposures of TEB and N_2/H_2 plasma was annealed at 800 °C for 30 min, while BN deposited on Si substrate by exposures of TDMAB and N_2/H_2 plasma was annealed in the temperature range of 300-900 °C for 30 min in N_2 atmosphere using ATV–Unitherm (RTA SRO-704) rapid thermal annealing system. Effect of post-growth annealing on structural, optical, morphological and chemical properties was studied using these samples.

2.4 Fabrication of AlN/BN Bishell HNFs by Combination of Electrospinning and ALD

A four-step fabrication process was utilized to fabricate the AlN/BN HNFs.

1) In the first step, nylon 6,6 templates was prepared by electrospinning.
2) AlN growth was carried out on electrospun polymeric nanofibrous template using alternating exposures of trimethyl aluminium (TMA) and N_2/H_2 plasma as aluminium and nitrogen precursors, respectively.
3) AlN HNFs have been obtained by removing the core polymeric template by calcination.
4) As a last step, BN has been deposited on AlN HNFs using TEB and N_2/H_2 plasma as alternating precursors for boron and nitrogen to obtain AlN/BN bishell HNFs.

2.4.1 Electrospinning of Nylon Nanofibrous Sacrificial Templates

Nylon 6,6 having 8 wt.% (w/v) was dissolved in formic acid by stirring for 3 h at room temperature, for each sample. The resulting homogeneous clear solution was placed in 10 ml syringes fitted with metallic needles having inner diameter of 0.8 mm. The syringes were fixed horizontally on the syringe pump (Model: SP 101IZ, WPI). The polymer solution was pumped with feed rate of 1 mL/h during electrospinning and the tip-to-collector distance was set to 10 cm. 15 kV was applied to the metal needle tip using high voltage power supply (Matsusada, AU Series) for the electrospinning of the polymer solution. The solvent evaporated on the way to the grounded stationary cylindrical metal collector (height: 15 cm, diameter: 9 cm) covered with a piece of aluminium foil. The randomly oriented electrospun nylon nanofibers were deposited onto Si wafer which was fixed on the aluminium foil. The electrospinning setup was enclosed

in a Plexiglas box and the electrospinning was carried out at 23 °C and 36% relative humidity.

2.4.2 Atomic Layer Deposition of AlN

200 cycle ALD growth of AlN was carried out on electrospun nanofibers at 100 °C in a Fiji F200-LL ALD reactor (Cambridge Nanotech Inc., Cambridge, MA), which is equipped with a stainless steel hollow cathode plasma source (Meaglow Ltd.), with a base pressure of 150 mTorr. Precursors utilized for the growth of AlN were TMA and N_2/H_2 plasma with argon (Ar) as the carrier and purge gas. One hollow cathode plasma assisted ALD (HCPA-ALD) cycle consisted of 0.06 s TMA pulse/10 s Ar purge/40 s N_2/H_2 plasma (50/50 sccm, 300 W)/10 s Ar purge.

2.4.3 Removal of Sacrificial Nanofibrous Polymeric Templates

AlN growth was followed by the calcination of AlN-coated nylon nanofibers in air ambient at 500 °C for 2 h in order to remove the polymeric core. Nylon polymer template decomposition procedure is based on high temperature calcination technique.

2.4.4 Low-Temperature Sequential CVD of BN

Following the calcination/ethanol treatment of AlN-coated polymeric nanofibers, AlN HNFs were introduced into the same ALD reactor and coated with BN at 450 °C to obtain AlN/BN bishell HNFs. 1000 growth cycles of BN was carried out utilizing TEB and N_2/H_2 plasma sequentially as boron and nitrogen precursors with Ar as carrier and purge gas. One growth cycle consisted of 0.12 s TEB pulse/20 s Ar purge/40 s N_2/H_2 plasma (50/50 sccm, 300 W)/20 s Ar purge. Precursor and plasma carrier gas flow rates were 30 and

100 sccm, respectively. Samples were taken out from the reactor through a load-lock and exposed to air as soon as the ALD reactor cooled down to 200 °C.

2.5 Characterization Methods

In SEM, specimen is bombarded by a focused beam of high energy electrons which is rastered across the surface of the specimen. This electron beam generates a variety of signals (secondary electrons, back scattered electrons, and characteristic X- rays), which are emitted from the area of specimen exposed to electron beam [75]. These signals provide valuable information about topography and composition of the sample. In this study, Nova NanoSEM (FEI) was used to reveal surface morphology, uniformity, and HNFs dimensions of the nanostructured samples. Prior to imaging, BN thin film and AlN/BN nanostructures were coated with 5 nm Au/Pd to eliminate the charging effect.

AFM is a high resolution scanning probe microscopy (SPM) that may be used to obtain micro- and nano-scale morphology of a wide range of samples, including both conductive and insulating materials [76]. In this study, surface morphologies of the BN thin films were revealed using an atomic force microscope (AFM) (XE-100E, PSIA, Suwon, Korea), operated in the contact mode.

XPS is a widely used technique to determine quantitative atomic composition of solid surface. Moreover, this technique provides other significant thin film material information such as elemental composition, chemical bonding state information, and uniformity of sample surface without the restriction on type of material being analyzed [77, 78]. In this work, elemental composition and chemical bonding states of the BN films and AlN/BN nanostructures were determined by XPS using Thermo Scientific K-Alpha spectrometer (Thermo Fisher Scientific, Waltham, MA) with a monochromatized Al Kα X-ray source. Sputter depth profiling was performed with a beam of Ar ions having an acceleration voltage and spot diameter-size of 1 kV and 400 µm, respectively.

X-ray crystallography is a technique, mainly used for identifying phases, atomic and molecular structure, unit cell lattice parameters, average crystallite size of nanocrystalline samples, and crystalline microstrain of a crystalline material [79-81]. In order to obtain information from very thin layers, grazing-incidence XRD (GIXRD) is preferred. In GIXRD, measurements are taken at very small incidence angles (typically smaller than 0.5°), which enables the small penetration depths and intensity enhancement at the surface. Incident angle, the beam path length, and the irradiated area are kept constant and only the detector rotates through the angular range during the collection of diffraction pattern. As a result, GIXRD can be utilized to analyze crystal structures ranging from a few to hundred nanometers below the surface of the solids. In this study, GIXRD patterns were recorded in an X'Pert PRO MRD diffractometer (PANalytical B.V., Almelo, Netherlands) using Cu Kα radiation. Data were obtained within the 2Theta range of 20-80° by the summation of ten scans, which were performed using 0.1° step size and 10 s counting time. Interplanar spacing (d_{hkl}) value for the (010) plane was calculated from peak position using the well-known Bragg's law. Lattice parameter *a* was roughly calculated by substituting d_{010} value in Eqn. 3.1, which relates the interplanar spacing (d_{hkl}), miller indices (*hkl*) and lattice parameters (*a* and *c*) for hexagonal crystals.

$$\frac{1}{d^2} = \frac{4}{3}\left(\frac{h^2+hk+k^2}{a^2}\right) + \frac{l^2}{c^2} \qquad (3.1)$$

By neglecting instrumental broadening and assuming that the observed broadening is only related to the size effect, crystallite size values for the as-deposited and annealed films were estimated from the (010) reflection using Eqn. 3.2, the well-known Scherrer formula

$$d = \frac{0.9\,\lambda}{B\cos\theta} \qquad (3.2)$$

where λ, *B* and θ are the wavelength of the radiation used (Cu K_α = 1.5418 Å), broadening (FWHM), and Bragg diffraction angle of the selected reflection, respectively.

Similar to SEM, TEM also utilizes an electron beam as imaging source. The major difference between SEM and TEM is that, TEM utilizes the transmitted electrons as an imaging source, while SEM detects the reflected electron from specimen surface. SEM focuses on samples surface only while TEM provides the details about internal structure, crystallization, and internal composition [82]. In this study, Tecnai G2 F30 TEM (FEI, Hillsboro, OR) was utilized for the high-resolution (HR) imaging of the BN thin film sample, which was capped with a 20 nm AlN layer prior to TEM sample preparation. AlN was deposited at 200 °C using HCPA-ALD. TEM sample was prepared by a Nova 600i Nanolab focused ion beam (FIB) system (FEI, Hillsboro, OR) at an acceleration voltage of 30 kV using various beam currents ranging from 50 pA to 21 nA. Damage layer was removed by FIB milling at a beam voltage of 5 kV. Elemental mapping was performed in TEM, using an energy dispersive X-ray spectrometer (EDXs). TEM, energy dispersive X-ray spectroscopy (EDXs), and selected area electron diffraction (SAED) analyses of AlN/BN nanostructures were performed using same TEM. TEM samples for AlN/BN nanostructures analysis were prepared by scratching hollow nanofibers from the substrate and dispersing them into ethanol, followed by sonification and drop casting onto copper grids.

Ellipsometry measures the change in polarization state of light reflected from the surface of the sample. The most common applications of ellipsometer include the measurement of film thickness and optical constants (refractive index and extinction coefficient) in UV, visible, and IR range. In this study, optical constants of the BN films were determined using a variable angle spectroscopic ellipsometer (V-VASE, J.A. Woollam Co. Inc., Lincoln, NE) which is equipped with rotating analyzer and xenon light source. The ellipsometric spectra were collected at three angles of incidence (65^o, 70^o, and 75^o) to yield adequate sensitivity over the full spectral range. Optical constants and film thicknesses were extracted by fitting the spectroscopic ellipsometry data. The numerical iteration was performed to minimize the mean-square error function using WVASE32 software (J.A. Woollam Co. Inc., Lincoln, NE). The

homogeneous Tauc-Lorentz (TL) function was used as an oscillator. In addition, data fitting was improved using the Bruggeman effective medium approximation at the film-air interface assuming 50% film and 50% voids. The absorption coefficient, $\alpha(\lambda) = \frac{4\pi k(\lambda)}{\lambda}$, was calculated from the k values determined from the ellipsometry data. Optical band gap (E_g) is expressed by the Eqn. 3.3 for direct band gap materials [83], which can be analytically extracted via extrapolation of the linear part of the absorption spectrum to $(\alpha E)^2 = 0$

$$\alpha E = A(E - E_g)^{1/2} \qquad (3.3)$$

Ultraviolet-visible (UV-VIS) spectrophotometry is used to measure the absorption or transmission spectra in the UV-VIS spectral region. Incident photon energy is absorbed by the electrons which can be excited to higher orbital's (such as π-electrons). In this study, spectral transmission measurements were performed with a UV-VIS spectrophotometer (HR4000CG-UV-NIR, Ocean Optics Inc., Dunedin, FL) in the wavelength range of 220-1000 nm relative to air.

Chapter 3

Results and Discussions

This chapter presents the experimental results of boron nitride (BN) thin film, growth recipe optimization, aluminium nitride (AlN)/BN hollow nanofibers (HNFs) fabrication process regarding electrospinning of polymeric templates, hollow cathode plasma-assisted atomic layer deposition (HCPA-ALD) of AlN, and sequential chemical vapor deposition (CVD) of BN. Moreover, optical, morphological, structural, and compositional characterization results of BN thin films and AlN/BN HNFs are also discussed in detail.

3.1 BN Thin Films Growth Using Sequential Exposure of Triethylboron (TEB) and N_2/H_2 Plasma

Deposition experiments of BN were carried out within the temperature range of 250-450 °C by the sequential injection of TEB and N_2/H_2 plasma. TEB belongs to alkyl (organometallic) class of precursors. Alkyls are known as true organometallic compounds as they contain direct metal-to-carbon bond, which

makes them very reactive. The primary and foremost reason for selecting TEB as boron precursor was its non-halide nature. As alkyl precursors don't possess halide metal bonds, their gaseous byproducts with hydrogen containing non metal reactants (N_2/H_2, NH_3) are typically saturated hydrocarbons which don't reabsorb and are generally inert. Also, steric hindrance effect in alkyl precursor is significantly less as compared to other classes of reactants as they don't have bulky ligands which contribute to steric hindrance [84,85]. This aspect of the alkyl precursors make them quite attractive for ALD processes as films deposited with alkyl precursors generally result in higher GPC with lower impurity contamination [86,87].

3.1.1 Optimization of Growth Parameters

In order to optimize growth parameters for deposition of BN thin films, pulse length of TEB, substrate temperature, Ar purge time, as well as the influence of post-deposition annealing are investigated. One growth cycle consisted of TEB pulse/20 s Ar purge/40 s, 50/50 sccm N_2/H_2 plasma (300 W)/20 s Ar purge. Flow rates of N_2/H_2 plasma, plasma power, and Ar purge length were kept constant for all the experiments. Hollow cathode plasma source was installed in our ALD system, capable of producing a maximum plasma power of 300 W. It was kept at its maximum power level throughout the experiments to make the N_2/H_2 radicals highly reactive towards TEB. Initially, same recipe was followed with 10 s of Ar purge length. Growth per cycle (GPC) was same for both the purge times. However, non uniform surface of substrate with small particles was observed for 10 s of Ar purge which was an indication that 10 s of purging was not enough to completely evacuate the reactor from unreacted excess precursor molecules and gaseous reaction by-products. This problem was solved by increasing the purge length to 20 s of Ar purge.

Dependency of GPC of BN on TEB pulse length at different temperatures is given in Fig. 3.1. At 250 °C GPC was 0.05 Å and it didn't change with

increasing pulse length of TEB precursor. It was an indication towards self limiting regime of ALD of BN with such a low growth rate. However, in contrast to ideal ALD process, subsequent experiments revealed that thickness of film remained constant with increasing number of growth cycles. Therefore, it was speculated that the BN film growth characteristic at 250 °C might be surface inhibited growth which was reported in the literature as well [88,89].

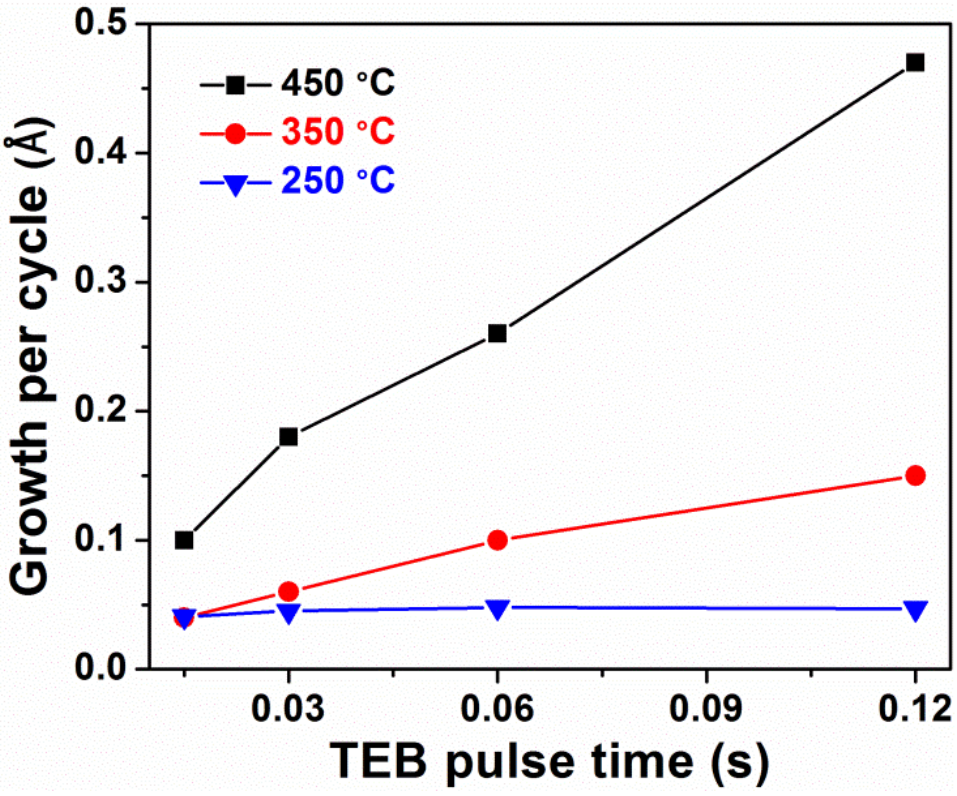

Figure 3.1: Effect of TEB dose on GPC at different temperatures. N_2 and H_2 flow rates, plasma power and purge time were kept constant.

At 350 °C, GPC was 0.10 Å for 0.06 s of TEB pulse length, which went up to 0.15 Å after increasing the TEB pulse length to 0.12 s. Reasonable GPC values were achieved at substrate temperatures higher than 350 °C. At 450 °C, GPC was 0.26 Å for 0.06 s of TEB pulse length, which increased to 0.47 Å for 0.12 s of TEB pulse length. GPC increases almost linearly with increasing TEB pulse length at 350 °C and 450 °C with no saturation, which points towards the possibility of thermal decomposition of TEB at temperatures higher than 250 °C. Thus, no self-limiting growth behavior for BN deposition has been

observed, indicating a CVD-like deposition mode with substrate temperatures above the possible ALD window. In order to further investigate this issue and understand the decomposition temperature, controlled experiments, where Si substrates have been exposed to 100 TEB pulses, were performed within the 250-450 °C range and the resulting surfaces were analyzed with XPS.

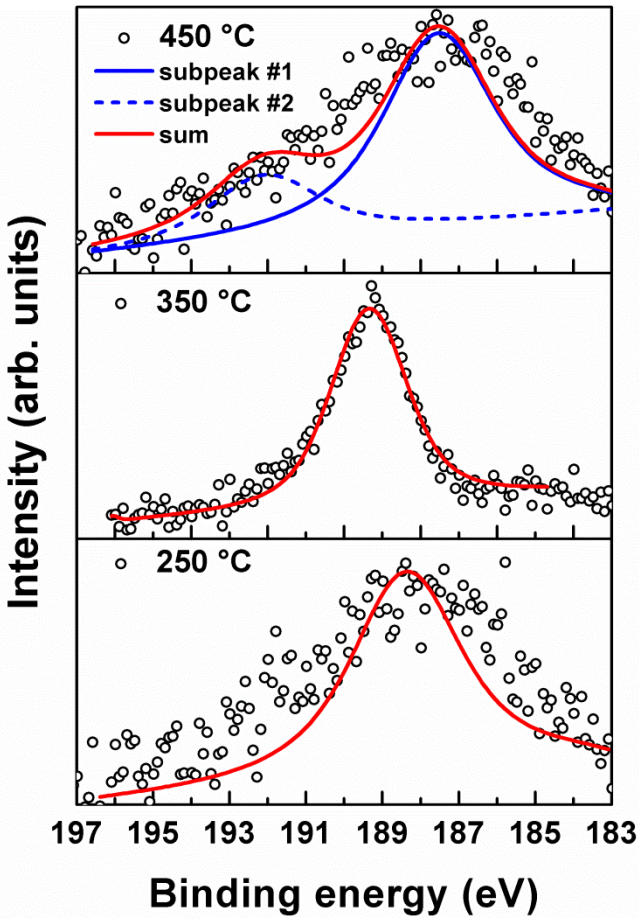

Figure 3.2: High-resolution B 1s scans obtained from Si surfaces, which have been exposed to 100 pulses of TEB at different temperatures.

High-resolution B 1s scan is given in Fig. 3.2, which has been analyzed for the possible bonding schemes of boron. B 1s HR-XPS spectrum gathered from the Si (100) surface exposed to 100 cycles of TEB at 350 °C was fitted by one peak with binding energy of 189.3 eV which indicates the presence of boron sub oxide (B_6O) [90]. While B 1s HR-XPS spectrum gathered from the Si (100) surface exposed to 100 cycles of TEB at 450 °C was fitted by two sub peaks

with binding energies of 187.5 and 192.1 eV which corresponds to B-B [91] bond and B-O [92] bond of boron oxide (B_2O_3), respectively. On the other hand, for the Si substrate exposed to TEB precursor at 250 °C, only B-C bond [93] is detected. TEB is an alkyl precursor which contains direct metal to carbon bond. B-C bond detection confirms that TEB is stable at 250 °C (no decomposition) and decomposition initiates at temperatures higher than 250 °C.

3.1.2 Characterization of BN Thin Films

3.1.2.1 Structural Characterization of BN Thin Film

The crystal structures of the as-deposited and annealed BN films were characterized by grazing incidence X-ray diffraction GIXRD. Figure 3.3(a) shows the GIXRD patterns of ~47 and ~15 nm thick BN films deposited on Si (100) substrates at 450 and 350 °C, respectively. The results revealed that BN films were polycrystalline with hexagonal structure (ICDD reference code: 98-002-7986). As seen from Fig. 3.3(a), the (010) reflection of the hexagonal phase is dominant, while the other two reflections of hexagonal phase, i.e., (002) and (111), are weakly pronounced. From 2θ position of the (002) reflection, the lattice parameter *c* was calculated for the film deposited at 450 °C. Interplanar spacing (d_{hkl}) of (002) planes was calculated from Bragg's law and it was inserted in Eqn. (3.1) to obtain the *c*-axis lattice parameter, which came out to be 0.71 nm. This value is fairly close to 0.67 nm, which is the ideal value for hBN. Since (010) peak in the GIXRD pattern is well defined, *a*-axis lattice parameter estimation would be more accurate as compared to *c*-axis lattice parameter estimation. From 2θ position of the (010) reflection, the lattice parameter *a* was calculated for the film deposited at 450 °C. Interplanar spacing (d_{hkl}) for the (010) plane was calculated from Bragg's law and it was inserted in Eqn. (3.1) to obtain the *a*-axis lattice parameter, which came out to be 0.25 nm. This value matches well with the ideal value (0.25 nm) of *a*-axis lattice parameter for hBN.

This shows the superiority of HCPA-ALD over thermal ALD for obtaining a predominantly hexagonal phase in BN films.

Figure 3.3(b) shows a comparison of the GIXRD patterns of the as-deposited and annealed BN thin films deposited at 450 °C. One can conclude that the intensity of (010) reflection increases and the full width at half maximum (FWHM) becomes slightly narrower after the post-deposition annealing. FWHM of the hBN film deposited at 450 °C was measured as 123 arc-minutes, which decreased to 106 arc-minutes after annealing. Figure 3.3(c) shows the comparison of GIXRD patterns of BN thin films deposited at 450 and 350 °C after annealing at 800 °C for 30 min. Again, (010) reflection of the hexagonal phase is dominant, while the other two reflections of hexagonal phase, i.e., (002) and (111), are weakly pronounced. By neglecting instrumental broadening and assuming that the observed broadening is only related to the size effect, crystallite size values for the as-deposited and annealed films were estimated from corresponding (010) reflections using the well-known Scherrer formula. The crystallite size calculation from Scherrer formula is summarized in Table 3.1. The crystallite size was found to be 4.4 nm for the film deposited at 450 °C, which slightly increased to 4.7 nm after annealing process at 800 °C for 30 min. On the other hand, It was found to be 3.7 nm for the films deposited at 350 °C, which increased to 6.0 nm after annealing process at 800 °C for 30 min.

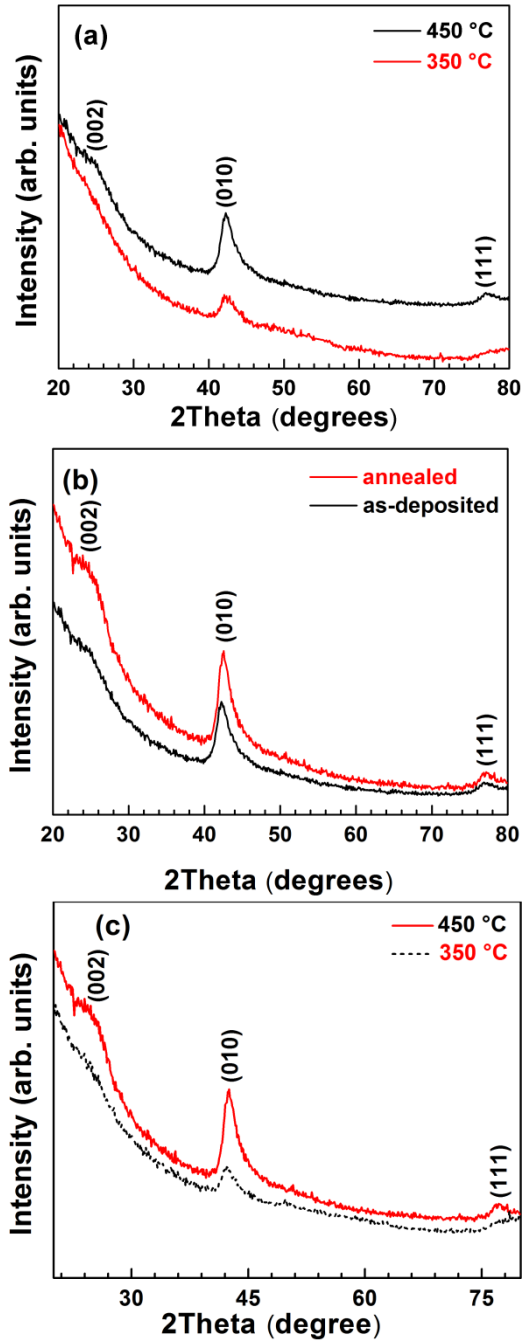

Figure 3.3: (a) GIXRD patterns of ~47 and ~15 nm thick BN films deposited on Si (100) substrates at 450 and 350 °C, respectively. (b) GIXRD pattern of the ~47 nm thick BN film deposited on Si (100) substrate at 450 °C: annealed vs. as-deposited. (c) GIXRD patterns of ~47 and ~15 nm thick BN films deposited on Si (100) substrates at 450 and 350 °C after annealing at 800 °C for 30 min, respectively.

Table 3.1: Crystallite size calculation from Scherrer formula for BN films deposited at 450 and 350 °C

	K	*λ(angstrom)*	*FWMH β(rad)*	*Θ*	*τ(Angstrom)*
Annealead 450 °C	0.9	1.54	0.031	21.27	47.34
As deposited 450 °C	0.9	1.54	0.036	21.12	44.58
Annealead 350 °C	0.9	1.54	0.024	21.12	60.87
As deposited 350 °C	0.9	1.54	0.040	21.02	37.02

Transmission electron microscope (TEM) experiments were carried out on a BN sample, which was prepared separately by the deposition of 2000 cycles on a Si (100) substrate at 450 °C with 0.12 s of TEB pulse length. Prior to TEM sample preparation, an AlN capping layer was deposited on top of the BN layer to preserve its crystal structure by providing a barrier layer against the damage of high energy Ga ions of the FIB system. The average thickness of BN was measured as ~90 nm from cross-sectional TEM measurements, which is in close agreement with the data obtained from spectroscopic ellipsometery. Figure 3.4(a) is the cross-sectional TEM image of BN thin film. It can be observed that the interface between AlN and BN is not distinct, which gives an indication of the non-uniform surface morphology of BN layer. Figure 3.4(b) shows the HR-TEM image indicating the polycrystalline structure and lattice fringes of hBN film. It is seen that hBN is composed of nanometer-sized crystallites.

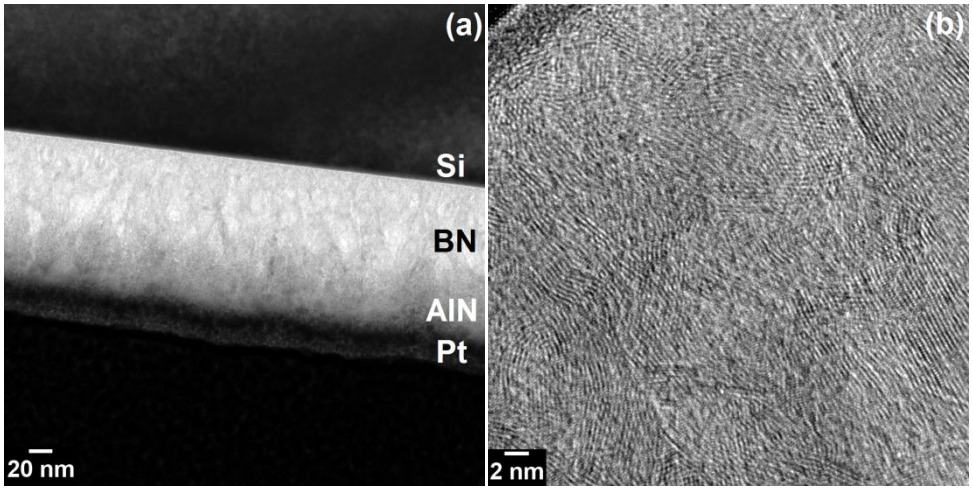

Figure 3.4: (a) Cross-sectional TEM image of AlN-capped ~90 nm thick BN thin film deposited at 450 °C on Si (100) substrate. (b) Cross-sectional HR-TEM image of the same sample.

Figure 3.5(a) shows energy dispersive X-ray spectroscopy (EDXs) elemental maps of B, Al and Si obtained from the AlN-capped BN thin film sample deposited on Si (100) at 450 °C. The elemental distribution is clarified by selecting a cross-sectional portion in the specimen and rastering the electron beam point by point over the selected portion of interest. The colorized maps show strong contrast among B, Al and Si, and they reveal the elemental distribution along the scanned area. The interface between Al and B is fuzzy, which confirms the intermixing of Al and B at the interface due to the non-uniform surface morphology of BN, which was observed in HR-TEM imaging as well. Figure 3.5(b) shows the selected area electron diffraction (SAED) pattern of the same AlN/BN sample. Polycrystalline diffraction rings of BN and AlN can be seen from this pattern. The interplanar spacing values were calculated from the diffraction rings that are associated with the BN layer (denoted on Fig. 3.5(b)), and found to be 2.19 and 1.23 Å, which are well matched with the theoretical values for (010) and (111) planes of hBN; i.e., 2.18 and 1.23 Å, respectively (ICDD reference code: 98- 002-7986). Note that the reciprocal lattice points correspond to diamond lattice of Si substrate. The corresponding interplanar spacing for (010) and (111) crystallographic planes confirm well with the GIXRD data explained above.

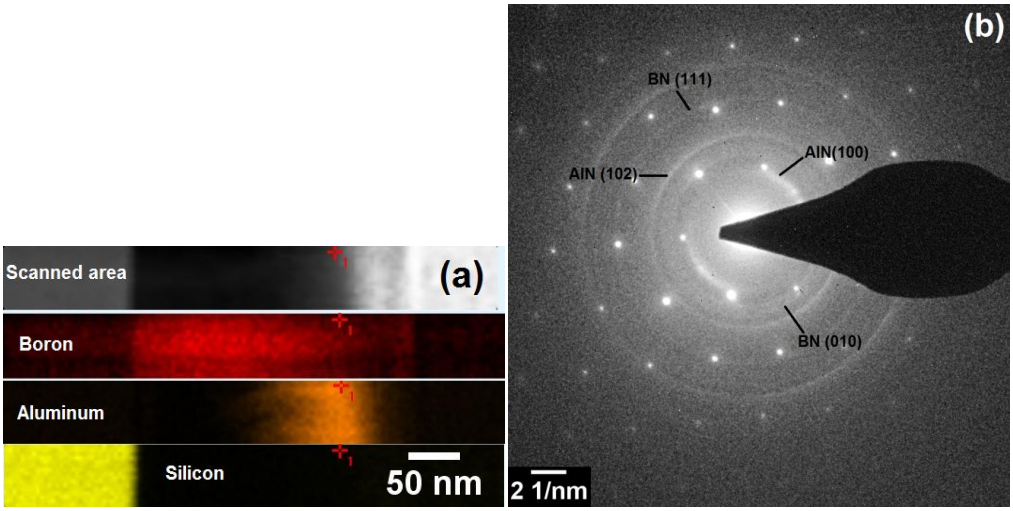

Figure 3.5: (a) Elemental map of the AlN-capped ~90 nm thick BN thin film deposited on Si (100) substrate at 450 °C. (b) SAED pattern of the same sample.

3.1.2.2 Compositional Characterization

In order to investigate the elemental compositions, chemical bonding states and impurity contents of the films, XPS was conducted on hBN films deposited on Si (100) substrates. Survey scans indicated the presence of boron, carbon, nitrogen, and oxygen with B 1s, C 1s, N 1s, and O 1s peaks located at 190.6, 284.6, 398.0, and 532.6 eV, respectively. Table 3.2 provides a comparison of the elemental compositions and the corresponding B/N ratios for as-deposited and annealed BN films. It illustrates that films are nearly stoichiometric with B/N ratios of ~1.05 to 1.12. An increase of 2-3 at.% was observed in the oxygen concentrations of films after annealing, which might be due to initiation of oxidation at the surfaces of BN films. Figure 3.6 (a) is the compositional depth profile of hBN thin film, which indicates the variation of atomic concentrations of boron, nitrogen, carbon, and oxygen along the etching direction from the air/hBN interface towards the hBN/Si (100) interface. Boron and nitrogen atomic concentrations were found to be constant in the bulk film. 15 at.% oxygen was detected at the film surface, which decreased to ~2 at.% in the bulk of the film, while carbon content was also around 2 at.% in the bulk of the BN film. The carbon impurity contents in the films might be originating from the ethyl groups of TEB, which did not react with the N_2/H_2 plasma and therefore remained in the growing film.

The high-resolution scans of B 1s and N 1s are given in Fig. 3.6 (b) and (c), respectively, which refer to the bulk film (t_{etch} = 720 s). FWHM and asymmetry of the peaks suggest that there are more than one type of bonding scheme for boron and nitrogen. The high-resolution XPS spectra were therefore analyzed to inspect the possible bonding schemes of the deposited hBN. B 1s HR-XPS spectrum gathered from the surface of a ~47 nm thick BN sample deposited on Si (100) substrate was fitted by two subpeaks with binding energies of 190.8 and 189.0 eV. In literature it has been reported that B1s HR spectrum exhibits binding energy of 190.8 eV [94] and 189 eV [95,97] for BN and B-C

bond in boroncarbonitride (BCN) films. Therefore, the subpeak detected at 190.8 eV can be safely attributed to the B-N bond, while the peak at 189.0 eV possibly indicates the presence of B-C bonding state of BCN. N 1s high-resolution spectrum given in Fig. 3(c) was fitted by two subpeaks located at 398.3 and 399.1 eV. In literature it has been reported that N1s HR spectrum exhibits binding energy of 399 eV [95,97] for N-C bond in boroncarbonitride (BCN) films. The sub peak at 398.3 eV [96] confirms the presence of BN, while the subpeak at 399.1 eV again indicates the formation of BCN.

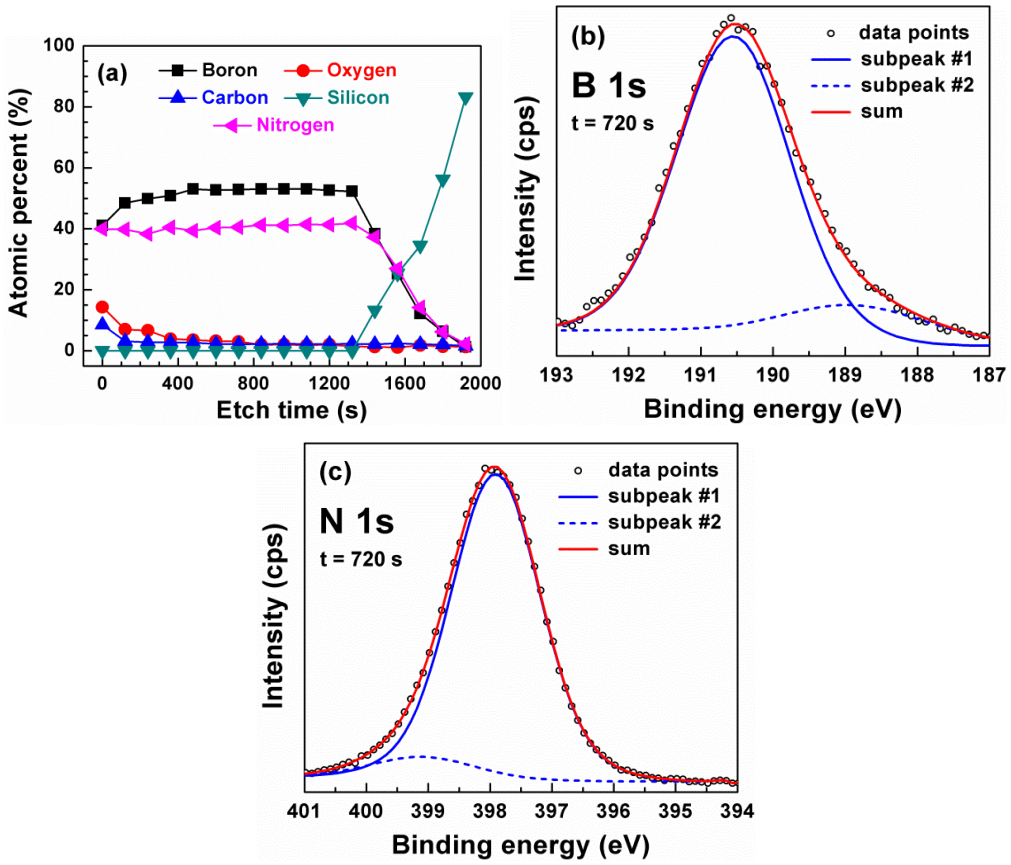

Figure 3.6: (a) Compositional depth profile of ~47 nm thick BN thin film deposited on Si (100) at 450 °C. (b, c) High-resolution B 1s and N 1s scans of the same sample. Data were collected after 720 s of Ar ion etching.

Table 3.2: Refractive indices of the hBN films deposited on Si (100) substrates at different temperatures.

Deposition temperature	Elemental composition (at.%)				B/N ratio
	B	N	O	C	
350 °C (as-deposited)	42.70	40.81	4.55	5.55	1.05
350 °C (annealed)	46.27	42.15	7.29	4.29	1.09
450 °C (as-deposited)	44.06	38.47	4.46	6.05	1.14
450 °C (annealed)	47.99	42.85	6.18	2.98	1.12

3.1.2.3 Morphological Characterization

Figure 3.7(a) shows plan-view SEM image of hBN film deposited on Si (100) substrate at 450 °C, while 3.7(b) shows the SEM image of the same sample after it has been annealed at 800 °C for 30 min. SEM analysis of the as-deposited sample reveals that the surface of the hBN thin film sample is not uniform with a rough, compact and three-dimensional (3D) curly surface morphology. It shows a branching feature with peculiar 3D nano-scale structures. SEM image of annealed sample (Fig. 3.7(b)), on the other hand, reveals that branched 3D nanostructures have mostly coalesced to form a more continuous and larger-grained but still non-uniform film surface. The presence of this branching feature is not well understood yet; however, one possible mechanism is that during the heterogeneous nucleation and growth of preferential crystal planes on the substrate, abundant deposition vapor in CVD mode might have created new deposition steps on the preceding BN nanosheets, which could have resulted in the outgrowth of this branching structure. At some later stage during the deposition, the branched nanostructure might have terminated upon colliding with other branches, resulting in a highly 3D nanostructured surface. Another possibility might be that upon exposure of abundant growth vapour, inter growth of nanosheets in different directions along the energetically favorable axis could have lead to this branched nanonetwork upon collision of different sheets [98].

Surface morphologies of the hBN thin films were further examined by AFM. Figure 3.8 (a, b) and (b, c) show the surface scans of the ~47 nm thick BN thin film sample before and after annealing at 800 °C for 30 min, respectively. Root-mean-square (rms) roughness of the as-deposited film was measured as 0.70 nm from a 1 μm×1 μm scan area. Film roughness increased to 0.83 nm after annealing.

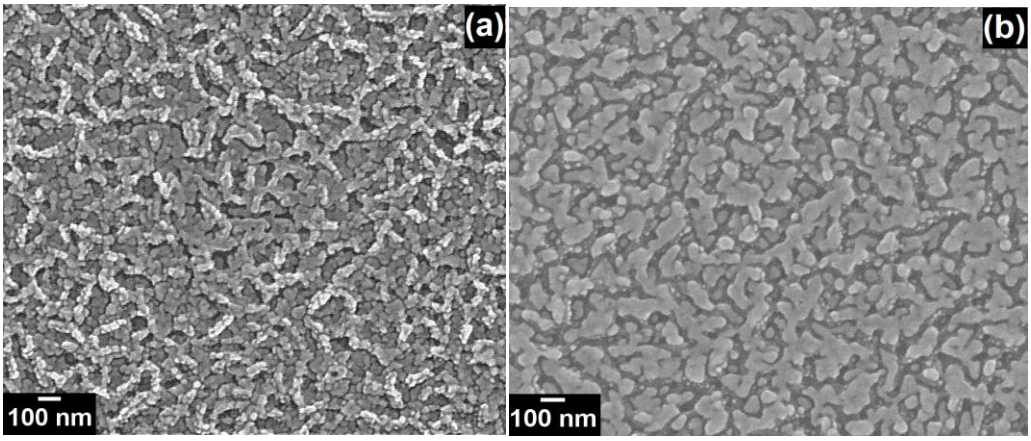

Figure 3.7: SEM images of ~47 nm thick BN thin film deposited on Si (100) substrate at 450 °C: (a) as-deposited, and (b) annealed.

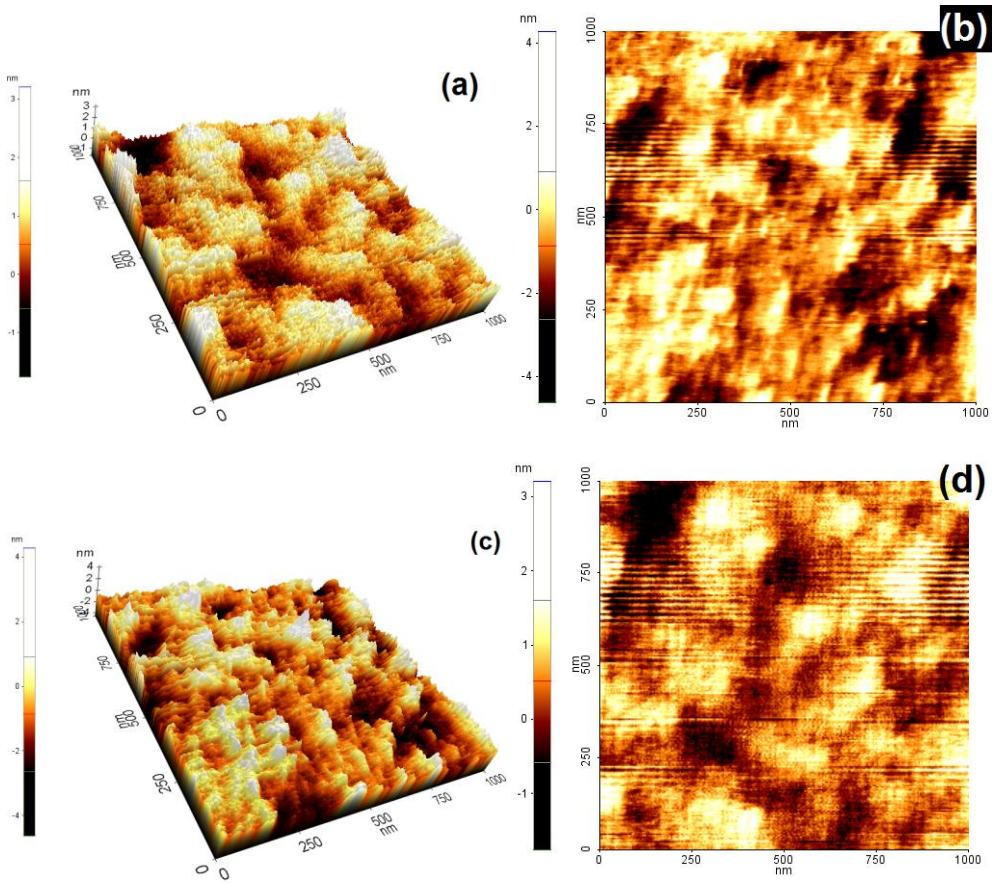

Figure 3.8: (a) Surface morphologies of ~47 nm thick BN thin film deposited on Si (100) substrate at 450 °C: (a), (b) as-deposited and (c), (d) annealed.

3.1.2.4 Optical Characterization

Normal incidence transmission spectra of BN thin film samples deposited on double side polished quartz substrates in the UV-VIS and NIR regions are presented in Fig. 3.9. The average transmittance was measured to be in the 91-93% range within the visible spectrum, very close to bare quartz transmission performance, which indicates that films are almost fully transparent in this wavelength region. Significant decrease in transmission was observed at UV wavelengths less than 280 nm, which is believed to be caused by the main band gap absorption. Optical band gap value was estimated from absorption edge of the films using Eqn. 3.3. The value of E_g was calculated from the inset

of Fig. 3.9, which shows the $(\alpha hv)^2$ vs. hv plot. The optical band gap was determined by extrapolating the straight line segment of the plot to abscissa as described earlier, and found to be ~5.25 eV. No change in optical band gap is observed for the annealed counterpart. The existence of a single slope in the graph is an indication that hBN features direct optical transitions. The value of E_g obtained in our work matches well with the E_g value measured for polycrystalline hBN films by Hoffman et al [99]. However, there is huge discrepancy in measured values of E_g. In literature, E_g value of hBN is largely dispersed in the range of 4.0-7.1 eV, which is explained by the differences in experimental methods used and quality of deposited hBN [100]. Initially, single crystal hBN was reported as a direct band gap material with an E_g value of 5.9 eV, but recently for polycrystalline hBN, it was demonstrated to be an indirect band gap material with an E_g value of 6.5 eV [101]. In view of numerous different reports, more experimental results regarding optical band gap of hBN are required.

Optical constants of the BN film were obtained by modeling the ellipsometric spectra in the wavelength range of 200-1000 nm. Figure 3.9(b) shows the variation of the refractive index as a function of incident photon wavelength. The refractive index decreases from 1.65 to 1.56 in the visible spectrum. Similar results have been reported in the literature for polycrystalline hBN films [102,103]. Furthermore, the extinction coefficient (k) decreased swiftly within the UV range and became almost zero at higher wavelengths, indicating the near-ideal transparency of the films in the visible spectrum. Refractive index value at 550 nm for the films deposited at 350 and 450 °C are summarized in Table 3.3.

Table 3.3: Refractive indices of the hBN films deposited on Si (100) substrates at different temperatures.

Deposition temperature	Refractive index, n at 550 nm
350 °C (as-deposited)	1.55
350 °C (annealed)	1.61
450 °C (as-deposited)	1.60
450 °C (annealed)	1.64

Refractive index value at 550 nm was measured as 1.55 for the BN film deposited at 350 °C, which increased to 1.61 after annealing the film. While, for the films deposited at 450 ^{o}C, refractive index values at 550 nm increased from 1.60 to 1.64 after annealing treatment. This slight increase might be attributed to structural enhancement (i.e., increase in grain size and/or film densification) upon annealing.

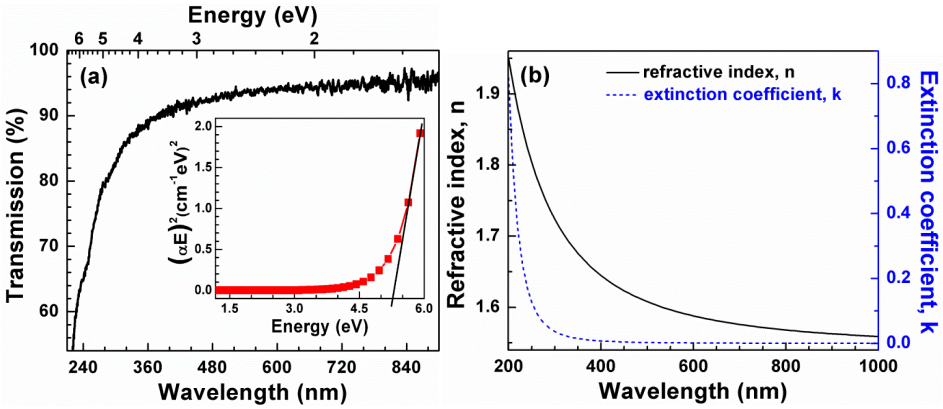

Figure 3.9: (a) Optical transmission, and (inset) absorption spectra of the ~47 nm thick BN thin film deposited on double side polished quartz. (b) Optical constants (refractive index and extinction coefficient) of the same sample

3.2 Fabrication of AlN/BN Bishell HNFs by Electrospinning and ALD

A four-step fabrication process was utilized to fabricate the AlN/BN HNFs. First, nylon 6,6 nanofibrous templates was prepared by electrospinning. Then, AlN growth was carried out on electrospun polymeric nanofibrous template using alternating exposures of trimethyl aluminium (TMA) and N_2/H_2 plasma as aluminium and nitrogen precursors, respectively. After that, AlN HNFs have been obtained by removing the core polymeric template by calcination. As a last step, BN has been deposited on AlN HNFs using TEB and N_2/H_2 plasma as alternating precursors for boron and nitrogen to obtain AlN/BN bishell HNFs. The deposition temperature of BN (450 °C) was not suitable for preserving the structure of polymeric templates, as polymer degradation starts around 350 °C. This compatibility issue was overcame by first depositing a layer of AlN at 100 °C, followed by a calcination process at 500 °C to efficiently remove the polymeric core, and finally BN deposition at 450 °C. BN growth is defined as sequential CVD instead of ALD which arise from the experimental evidence based on XPS studies confirming that TEB decomposition initiates at temperatures above 350 °C. Due to precursor decomposition, film growth is decomposition-limited which deviates from the ideal self-limiting ALD growth character and gas-phase CVD reactions start to occur which leads to precursor dose-dependent non-saturating growth behavior. Within the CVD regime, a growth temperature of 450 °C is selected, as reasonable growth per cycle (GPC) values were only observed at temperatures above 350 °C.

3.2.1 characterization of AlN/BN Bishell HNFs

3.2.1.1 Morphological Characterization

Electrospun nylon 6,6 nanofibers have been used as templates for the fabrication of AlN/BN bishell HNFs. Figure 3.10 shows SEM image of electrospun nylon 6,6 nanofibers which reveals the smooth morphology of nanofibers with uniform diameters. The average diameter of electrospun nylon 6,6 nanofibers was ~100. AlN has been deposited using HCPA-ALD where appropriate wall thickness has been achieved by using 200 growth cycles. AlN coated electrospun nylon 6,6 nanofibers were calcined at 500 °C for 2 hours in air ambient for removing nylon 6,6 polymer core. Highly conformal and uniform hollow AlN nanofibers were obtained and after calcination [Fig. 3.11(a, b)] by virtue of self terminating chemical reactions of HCPA-ALD. These AlN nanofibers are ideal replicate of electrospun nylon 6,6 templates with hollow morphology.

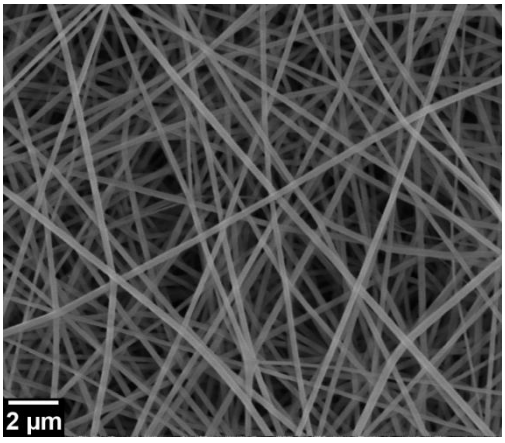

Figure 3.10: SEM images of electrospun Nylon 6,6 nanofiber templates having ~100 nm average fiber diameter.

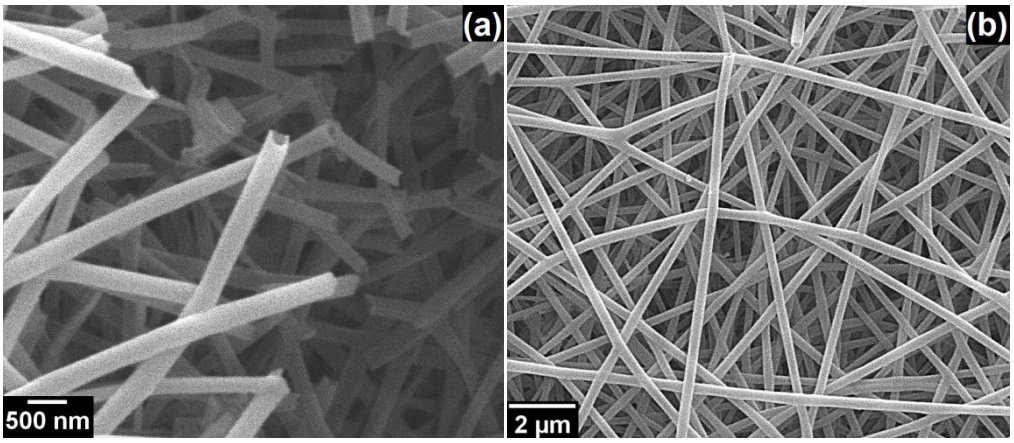

Figure 3.11: SEM images of hollow AlN HNFs synthesized by depositing 200 cycles AlN on nylon 6,6 templates followed by calcination.

1000 cycles of BN was grown at 450 °C on AlN HNFs to obtain AlN/BN bishell HNFs. Figure 3.12(a, b) depicts SEM images of AlN/BN HNFs after depositing BN on AlN HNFs originally based on nylon templates. SEM images reveal that integrity of structure was preserved after BN deposition and three-dimensional (3D) network of AlN/BN bishell HNFs have been successfully obtained. Flexibility of AlN/BN HNFs remain preserved and hollow morphology could only be observed from edges of the sample. Figure 3.12(c) is the high magnification SEM image of AlN/BN HNFs which reveals that surface morphology of AlN/BN fibers was not uniform and highly rough nanoneedle like surface morphology has been obtained. This nanoneedle like morphology was further confirmed by TEM images as well.

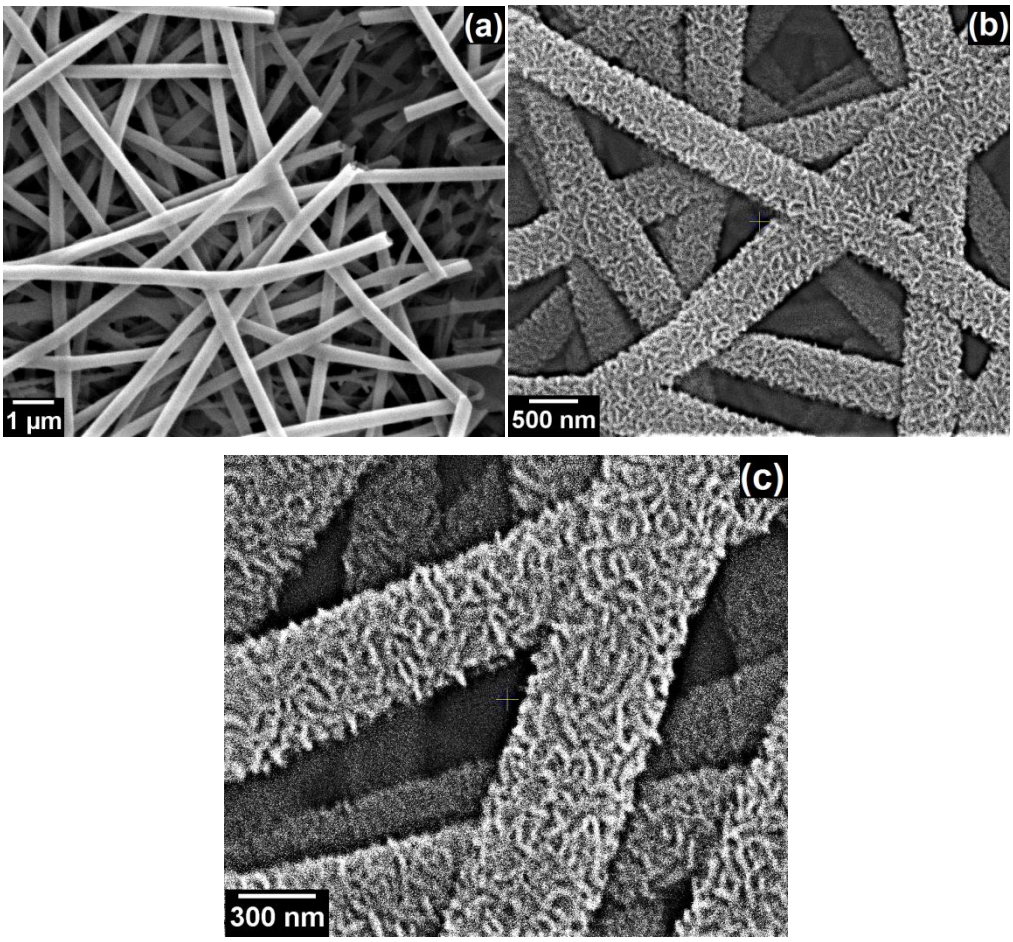

Figure 3.12: SEM images of AlN/BN bishell HNFs obtained after depositing BN on AlN fiber templates.

3.2.1.2 Structural Characterization

Representative bright field TEM images of AlN HNFs prepared by 200 cycles of AlN growth on electrospun nanofibrous templates, followed by calcination at 500 °C for 2 h are given in Fig. 3.13(a) and (b).

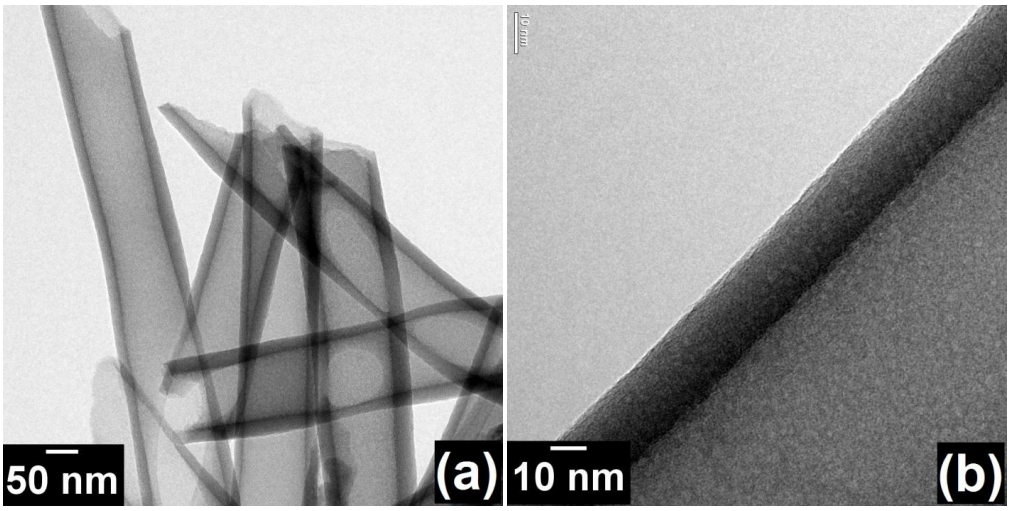

Figure 3.13: Bright field TEM image of (a) AlN hollow nanofibers synthesized by using nylon 6,6 template having an inner fiber diameter of ~100 nm with wall thickness of ~20nm (b) an individual AlN hollow nanofiber.

Wall thickness of AlN was measured as ~20 nm, which is highly conformal and uniform. Figures 3.14(a), (b), and (c) show TEM images of AlN/BN bishell HNFs. BN radially grows on the surface of AlN and surface of BN is terminated by highly rough nanoneedle like morphology. The average thickness of BN nanoneedle terminated layer is ~35nm, obtained after carrying out 1000 growth cycles of BN on AlN HNFs. Bishell hollow structure with separate AlN and BN layers can be clearly observed. Lattice fringes corresponding to different crystallographic planes of BN can be observed in high-resolution TEM image [Fig. 3.14(c)], which reveals that BN has a polycrystalline layered structure. Figure 3.15 shows energy dispersive X-ray spectroscopy (EDXs) elemental mapping of boron, aluminium and nitrogen from an individual AlN/BN HNF. The distribution of elements is clarified by selecting a cross-sectional portion in the specimen and rastering the electron beam point by point over the selected portion of interest. The colored maps show strong contrast among boron, aluminium, and nitrogen, and they reveal the elemental distribution along the scanned area. Nitrogen and boron are uniformly distributed along the scanned area while uniform aluminium distribution can be seen at the inner shell of the hollow nanofiber. It confirms the successful formation of AlN/BN bishell hollow nanofiber networks with a distinct interface between AlN and BN.

SAED pattern of AlN/BN HNFs (Fig. 3.16) exhibited several polycrystalline diffraction rings representing hexagonal BN (h-BN) and hexagonal AlN (h-AlN) phases. The analysis of SAED pattern has been summarized in Table 3.4 which compares measured and theoretical values for h-BN and h-AlN crystallographic planes. Reflections from the (010) and (111) crystallographic planes are detected for h-BN while (100) and (102) reflections are detected for h-AlN. Theoretical and experimental interplanar spacing (d_{hkl}) values are fairly close to each other for the corresponding crystallographic planes of h-BN and h-AlN.

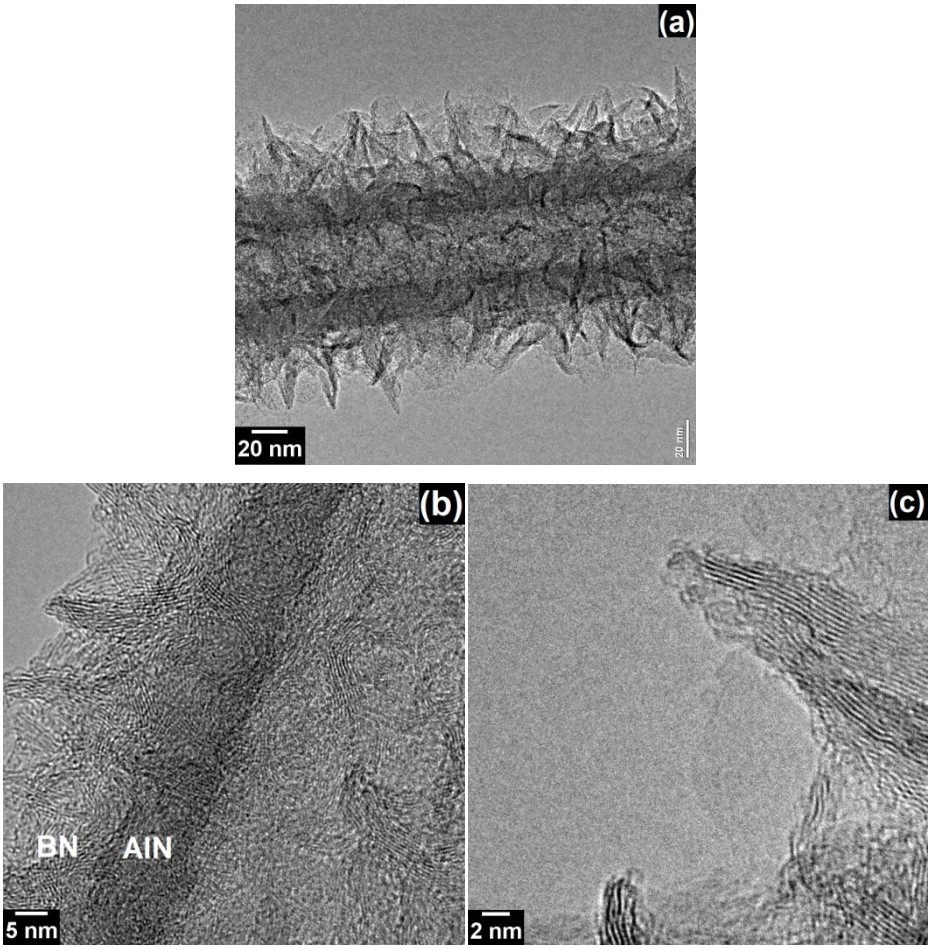

Figure 3.14: (a, b) Bright field TEM image of AlN/BN hollow nanofibers having an inner fiber diameter of ~100 nm with wall thickness of ~20 and ~35 nm of AlN and BN respectively, and (c) high resolution TEM images of BN nanoneedle like structure.

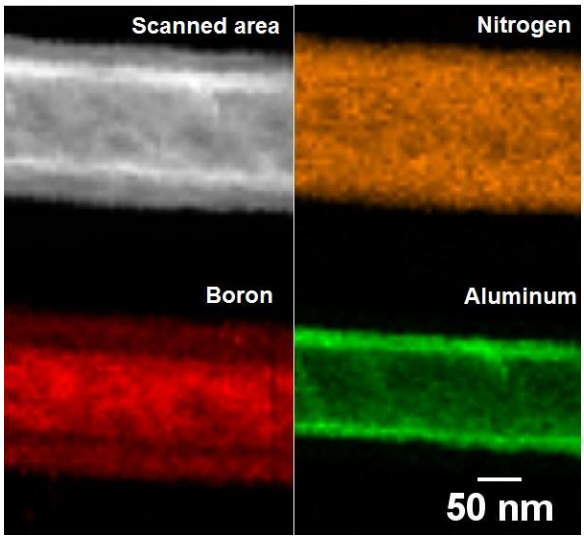

Figure 3.15: EDXs elemental mapping of AlN/BN bishell HNFs revealing elemental distribution of elements along the scanned area.

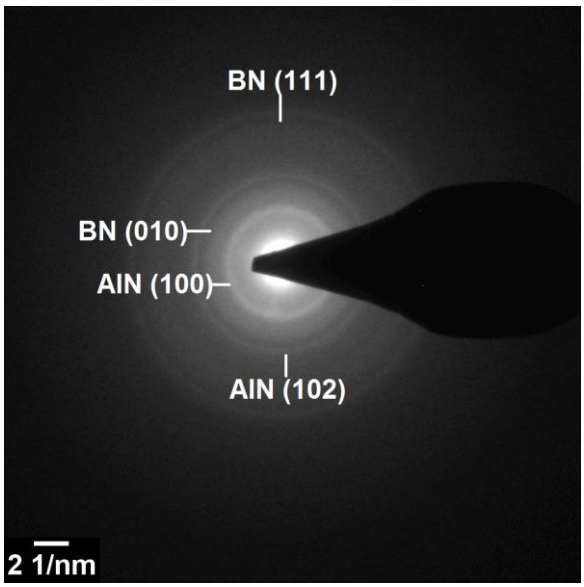

Figure 3.16: SAED pattern of AlN/BN bishell HNFs.

Table 3.4: SAED results of AlN/BN bishell HNFs, comparison between measured and theoretical values of interplanar spacing (d_{hkl}) with corresponding crystallographic planes.

Diameter	**Interplanar spacing, d_{hkl} (Å)**		**Corresponding material**	**Corresponding plane, (*hkl*)**
(nm^{-1})	Calculated	Theoretical		
7.381	2.7096	2.6950[a]	AlN	100
9.152	2.1853	2.1737[b]	BN	010
11.034	1.8125	1.8290[a]	AlN	102
16.204	1.2342	1.2334[b]	BN	111

[a] Hexagonal AlN, ICDD reference code: 00-025-1133.
[a] Hexagonal BN, ICDD reference code: 98-002-7986.

3.2.1.3 Compositional Characterization

In order to investigate the chemical composition, bonding states and impurity content of the films, XPS was conducted on AlN/BN bishell HNFs synthesized using electrospun nylon nanofibers as template. Survey scans from the surface of AlN/BN bishell HNFs indicated the presence of B, C, N, and O, while from the surface of AlN HNFs, it indicated the presence of Al, C, N, and O. It must be noted that the large spot size of X-ray beam (400 μm) interacts with a large number of HNFs and collects data from ~5-10 nm range in survey scan. This data probably represents outer surface of HNFs and some part of the inner surface of HNFs which is exposed to X-ray beam through the openings of outer shell layer. Table 3.5 shows elemental atomic percentages obtained from survey scan results of AlN/BN bishell and AlN HNFs. It illustrates that AlN/BN HNFs are nearly stoichiometric with relatively low impurity content. Considerably large amount of O in AlN HNFs is possibly due to oxidation of AlN upon annealing in air ambient. On the other hand, relatively low oxygen content (4.15 at.%) manifested in AlN/BN HNFs might be due to high oxidation resistance of BN. Moreover, stainless steel hollow cathode plasma (HCP) source used in this study was found as an alternative to inductively coupled RF-plasma (ICP) source for avoiding the oxygen contamination problem in PA-ALD-grown III-nitride thin films. Low oxygen content in AlN/BN bishell HNFs can be partly attributed to the superiority of HCP in comparison with ICP. The 11.5 and 14.7

% C present in AlN and AlN/BN HNFs, respectively, might correspond to surface contamination and residues left after calcination. The B 1s and N 1s high-resolution XPS scans obtained from AlN/BN bishell HNFs are shown in Fig. 3.17(a) and (b), respectively. The XPS spectra were analyzed to inspect the possible bonding schemes within the HNFs. Both B 1s and N 1s high-resolution XPS spectra were fitted by merely almost-symmetrical single peaks with binding energies of 190.7 [94] and 398.4 [96] eV, respectively, which confirm not only the presence of BN, but the low-impurity concentration as well.

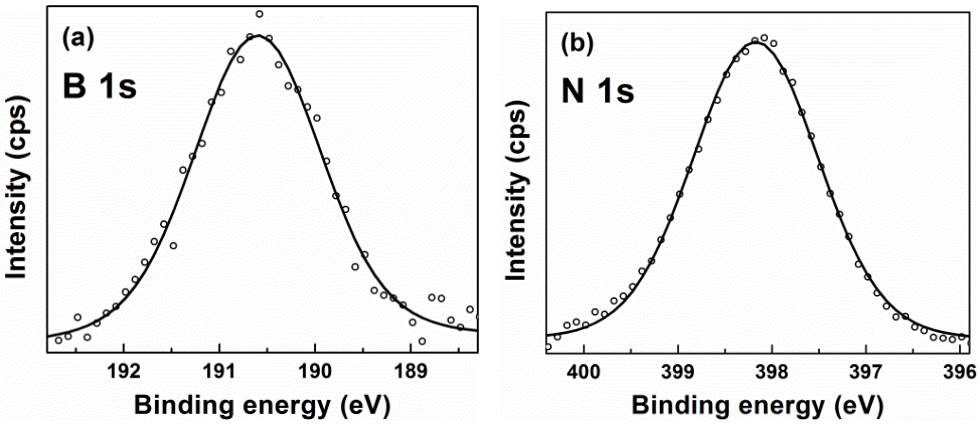

Figure 3.17: (a) B 1s and (b) N 1s high resolution XPS scans of AlN/BN HNFs based on nylon 6,6 templates.

Table 3.5: XPS survey scan results of AlN and AlN/BN bishell HNFs.

Sample	**Elemental composition (at.%)**				
	B	N	Al	O	C
AlN/BN HNFs	43.26	41.05	-	4.15	11.54
AlN HNFs	-	7.15	41.25	36.86	14.74

3.3 BN Deposition Using Sequential Exposures of Tris(dimethyl)amidoboron (TDMAB) and N_2/H_2 as Boron and Nitrogen Precursors.

BN growth experiments were performed in the range of 50 to 400 °C by utilizing TDMAB and N_2/H_2 as boron and nitrogen precursors. No film growth was observed at 200 °C, 300 °C, and 400 °C which was confirmed by ellipsometery and XPS. Possible reason for having no growth at all is desorption of monolayers at these temperatures. Growth temperature was then reduced to 50 °C. Sample was inspected with the ellipsometery for thickness measurement and optical constants estimation. The thickness of the film deposited at 50 °C after 800 cycles of growth is 25 nm. Refractive index of the as deposited film at 50 °C is found to be 1.57 which is close to reported values of refractive index for polycrystalline hBN [102,103].

The film was then annealed at three different temperatures for 30 min inorder to check the effect of post growth annealing on film structural and optical properties. The refractive index of the film increases progressively with increase in annealing temperature and finally reaches at 1.81 for the film annealed at 900 °C as shown in Table 3.6. This might be an indication of increased crystallinity in the films with annealing. However, in contrast to the above hypothesis, subsequent GIXRD measurements revealed that films were amorphous. In this regard, TEM investigations might help to conclude the effect of annealing. One notable difference is the decrease in thickness of the films with the increase in annealing temperature. The film was further characterized by XPS measurements.

Table 3.6: measurement of thickness and refractive index of as deposited and annealed films

Sample	Thickness	Refractive index
As deposited at 50 °C	25nm	1.57
Annealead at 300 °C	18nm	1.61
Annealead at 600 °C	16nm	1.64
Annealead at 900 °C	12nm	1.81

Table 3.7 presents the atomic percentages of different elements in the film deposited at 50 °C and after annealing at 900 °C. It can be seen that B/N at.% ratio is close to unity in all the samples. Caron content is 24.2 at. % at the surface of as deposited sample at 50 °C which is significantly decreased in the bulk (3.9 at.%). Carbon content at the surface might be attributed to surface contamination while relatively small carbon concentration in the bulk of the sample might be due to incomplete reaction of TDMAB with N_2/H_2 plasma. Large bulky ligands of TDMAB might be a reason for the incomplete reaction. Si at. % of 6.58 and 14.29 was seen in the surface and bulk scans of the annealed films, respectively, which was arising from the silicon substrate. Silicon atomic signals confirm the thickness decrease in the annealed film as compare to as deposited film. Oxygen concentration is quite high in all the samples. The reason for the large oxygen content in all the samples is still unknown. Further experiments with optimization of pulse length of TDMAB and N_2/H_2 plasma might help in clarifying this issue.

Table 3.7: XPS survey scan results from the surface and bulk of as deposited and annealed film.

Sample	N1s (at. %)	B1s (at. %)	C 1s (at. %)	O1s (at. %)	Si (at. %)
BN deposited at 50 °C (surface scan)	22.11	20.67	24.22	32.99	-----
BN deposited at 50 °C (bulk scan)	20.84	29.31	3.9	44.95	-----
BN annealed at 900 °C (surface scan)	24.2	26.3	11.93	30.99	6.58
BN annealed at 900 °C (bulk scan)	18.92	19.83	4.84	42.13	14.29

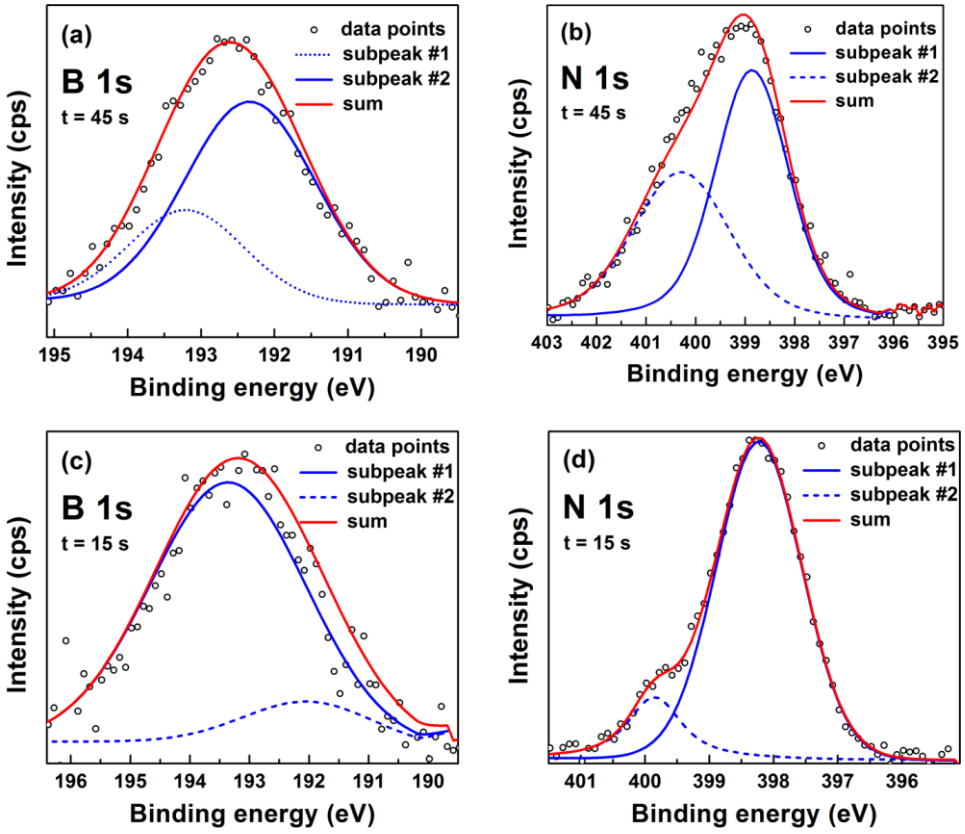

Figure 3.18: HR-XPS scans of (a) and (b) B1s and N1s from bulk of as deposited film at 50 °C, respectively, (c) and (d) B1s and N1s from bulk of annealed film at 900 °C, respectively

The high-resolution XPS spectra of as deposited and annealed samples were analyzed to inspect the possible bonding schemes of the deposited films. B 1s HR-XPS spectrum obtained from the surface of ~25 nm thick BN sample

deposited on Si (100) substrate was fitted by two subpeaks with binding energies of 192.1 and 193.2 eV. The hBN and boron oxide (B_2O_3) peaks appear in the range of 190.8-192.2 eV [94,104] and 192.5-193.7 eV [105], respectively. Therefore, the subpeak detected at 192.1 eV might be attributed to the B-N bond, while the peak at 193.2 eV possibly indicates the presence of B_2O_3. In literature, binding energy values for N-B bonds within the N 1s spectral range is given as 398.2 eV [96]. While binding energy value for C-N bond for different compounds of nitrogen and carbon are reported in the range of 399-401.7 eV [106]. N 1s high-resolution spectrum is given in Fig. 3.18 (b), which was fitted by two subpeaks located at 398.6 and 400.2 eV. The former might corresponds to the B-N bond, which gives an indication of the presence of BN, while the latter peak might be attributed to N-C bonding state.

B 1s HR-XPS spectrum obtained BN sample annealed at 900 °C deposited on Si (100) substrate [Fig. 3.18(c)] was fitted by two subpeaks with binding energies of 192.1 and 193.3 eV. The subpeak detected at 192.1 eV again possibly indicates the B-N bond, while the peak at 193.3 eV indicates the presence of B_2O_3. The percentage of B-O bonding in the annealed sample seems to be much higher as compare to as deposited sample which is indicated by the large area under the peak of B_2O_3. This might be due to oxidation of BN during high temperature (900 °C) annealing. N 1s high-resolution spectrum obtained from the BN sample annealed at 900 °C is given in Fig. 3.17 (d) was fitted by two subpeaks located at 398.1 and 399.9 eV. The former corresponds to the B-N bond, which indicates the presence of BN, while the latter peak might be attributed to N-C bonding state.

Chapter 4

Summary and Future Directions

Hexagonal boron nitride (hBN) thin films were deposited on silicon and quartz substrates using triethylboron (TEB) and N_2/H_2 plasma in hollow cathode plasma-assisted atomic layer deposition (HCPA-ALD) reactor. HCPA-ALD reactor have been used for the first time to deposit hBN films with non halide precursors which resulted in crystalline hBN films with low impurity content. Appreciable growth per cycle (GPC) values were only observed at substrate temperatures above 350 °C. At 350 °C, GPC was 0.15 Å for TEB pulse length of 0.12 s, while it was 0.47 Å at 450 ^{o}C for the same TEB pulse length. GPC did not saturate with increasing TEB doses, indicating the thermal decomposition of the boron precursor. Additional XPS studies based on exposure of 100 cycles of TEB on Si at different temperatures also indicated decomposition of precursor at 350 and 450 °C. Hence, it was concluded that growth regime is chemical vapour deposition (CVD) at 350 and 450 °C. BN thin films synthesized in CVD regime were polycrystalline with hexagonal structure as determined by GIXRD and HR-TEM. B 1s and N 1s HR-XPS scans further confirmed the presence of BN with peaks located at 190.8 and 398.3 eV, respectively. Rms surface roughness of the as-deposited BN thin film at 450 °C was measured as 0.70 nm from a 1 μm×1 μm scan area. Films exhibited an optical band edge at ~5.25 eV and high

transparency (>90%) in the visible region of the spectrum. Post-deposition annealing resulted in a slight improvement in crystallinity and led to an increase in crystallite size, refractive index and surface roughness of BN thin films deposited at 450 °C. This study represents the first demonstration of controlled deposition of hBN films within a HCPA-ALD reactor at relatively low substrate temperatures using sequential injection of non-halide triethylboron (TEB) and N_2/H_2 plasma as the boron and nitrogen precursors, respectively. Moreover, another nonhalide alternative precursor named tris(dimethyl)amidoboron (TDMAB) was studied for deposition of BN films. Initial experiments were performed using TDMAB and N_2/H_2 plasma as boron and nitrogen precursor. Film growth was only observed at low temperatures (50 °C) with high impurity content which was verified by XPS.

Effectiveness of the ALD method for coating ceramic nanostructured BN samples with high surface areas was also demonstrated within the scope of this thesis. Precisely controlled aluminium nitride (AlN)/BN bishell hollow nanofibers (HNFs) were fabricated by depositing AlN on electrospun polymeric nanofibrous template by HCPA-ALD, which was followed by the removal of polymeric template by calcination or ethanol treatment and low-temperature sequential plasma-assisted CVD of BN, respectively. SEM and TEM studies have shown a 3D network of AlN/BN nanofibers which imitated the shape and dimensions of electrospun nanofibers. HCPA-ALD grown AlN layer was conformal and uniform as a result of self-terminating gas-solid reactions occurring at the nanofiber surface, while a branched and rough 3D surface morphology with nanoneedle crystallites has been observed for the CVD grown BN outer layer. Synthesized AlN/BN bishell HNFs were found to be polycrystalline with a hexagonal structure along with low-impurity content. The results of this study show that the combination of electrospinning and plasma-assisted low-temperature ALD/CVD can produce highly-controlled multi-layered bishell nitride ceramic hollow nanostructures. Electrospinning parameters can be controlled to achieve nanofibrous templates with different

average fiber diameters and self-limiting reactions of PA-ALD provide precise control over the wall thicknesses of AlN and BN layers with sub-nanometer accuracy. Such high surface area nanostructured AlN/BN coatings might find potential use in composite reinforcement, chemical sensing, and gas adsorption.

As a possible follow up of above study, following potential future research directions are given below.

- Growth recipe using TDMAB precursor can be optimized for deposition of crystalline BN with low impurity content. In this regard, growth parameters such as pulse lengths of both precursors, growth cycles, and deposition temperature needs to be optimized.
- HCPA-ALD of $B_xGa_{1-x}N$ and $B_xIn_{1-x}N$ thin films via digital alloying using TEB, trimethylgalium (TMG), and cyclopentadienylindium (CpIn) as boron, gallium and indium precursors, respectively.
- Growth recipe optimization to obtain $B_xGa_{1-x}N$ and $B_xIn_{1-x}N$ thin films alloys of desired electrical/optical properties.
- Demonstration of the electronic and optoelectronic device applications of HCPA-ALD-grown $B_xGa_{1-x}N$ and $B_xIn_{1-x}N$ alloys; i.e., transistors, resistive memories, photodetectors, etc.

Bibliography

[1] T. Suntola and J. Antson, US Patent 4.058, 430, 1977.

[2] A.M. Shevjakov, G.N. Kuznetsova, and V.B. Aleskovskii, *Chemistry of High-Temperature Materials*, Proceedings of the Second USSR Conference on High-Temperature Chemistry of Oxides, Leningrad, 1995.

[3] S. M. George, "Atomic layer Deposition: an overview," *Chemical Reviews*, vol. 110, no. 1 pp. 111-131, 2010.

[4] M. de Keijser and C. van Opdorp, "Atomic layer epitaxy of gallium arsenide with the use of atomic hydrogen," *Applied Physics Letters*, vol. 58, no. 11, pp. 1187-1189, 1991.

[5] R. L. Puurunen, "Surface chemistry of atomic layer deposition: A case study for the trimethyl aluminium/water process," *Journal of Applied Physics*, vol. 97, pp. 121301-121351, 2005.

[6] M. Leskela and M. Ritala, "Atomic layer deposition (ALD): from precursors to thin film structures," *Thin Solid Films*, vol. 409, pp. 138–146, 2002.

[7] R. L. Puurunen, "Growth per cycle in atomic layer deposition: a theorethical model," *Chemical Vapor Deposition*, vol. 9, no. 5, pp. 249-257, 2003.

[8] R. L. Puurunen, A. Root, S. Haukka, E. I. Iiskola, M. Lindblad, and A. O. I. Krause, "IR and NMR study of the chemisorption of ammonia on trimethyl aluminium-modified silica," *Journal of Physical Chemistry B*, vol. 104, no. 28, pp. 6599-6609, 2000.

[9] R. L. Puurunen, M. Lindblad, A. Root, and A. O. I. Krause, "Successive reactions of gaseous trimethyl aluminium and ammonia on porous alumina," *Physical Chemistry Chemical Physics*, vol. 3, pp. 1093-1102, 2001.

[10] S. Haukka, E. L. Lakomaa, and A. Root, "An IR and NMR study of the chemisorption of titanium tetrachloride on silica," *Journal of Physical Chemistry*, vol. 97, no. 19, pp. 5085-5094, 1993.

[11] A. Kytokivi, E. L. Lakomaa, A. Root, H. Osterholm, J. P. Jacobs, and H. H. Brongersma, "Sequential saturating reactions of $ZrCl_4$ and H_2O vapors in the modification of silica and γ-Alumina with ZrO_2," *Langmuir*, vol. 13, no. 10, pp. 2717-2725, 1997.

[12] A. Kytokivi, J. P. Jacobs, A. Hakuli, J. Merilainen, and H. H. Brongersma, "Surface characteristics and activity of chromia/alumina catalysts prepared by atomic layer epitaxy," *Journal of Catalysis*, vol. 162, no. 2, pp. 190-197, 1996.

[13] A. Hakuli, A. Kytokivi, and A. O. I. Krause, "Dehydrogenation of i-butane on CrO_x/Al_2O_3 catalysts prepared by ALE and impregnation techniques," *Applied Catalysis A*, vol. 190, no. 1-2, pp. 219-232, 2000.

[14] V. A. Tolmachev and Z. P. Khim, *Russian Journal of Applied Chemistry*, vol. 55, pp. 1410, 1982.

[15] M. N. Tsvetkova, I. M. Yur'evskaya, A. A. Malygin, S. I. Koltsov, Y. I. Skorik, and Z. P. Khim, *Russian Journal of Applied Chemistry*, vol. 55, pp. 256, 1982.

[16] S. K. Gordeev, E. P. Smirnov, S. I. Koltsov, and Z. O. Khim, *Russian Journal of General Chemistry*, vol. 52, pp. 1468, 1982.

[17] H. Nohira, W. Tsai, W. Besling, E. Young, J. Petry, T. Conard, W. Vandervorst, S. De Gendt, M. Heyns, J. Maes, et al., "Characterization of ALCVD-Al_2O_3 and ZrO_2 layer using X-ray photoelectron spectroscopy," *Journal of Non-Crystalline Solids*, vol. 303, no. 1, pp. 83-87, 2002.

[18] A. Satta, J. Schuhmacher, C. M. Whelan, W. Vandervorst, S. H. Brongersma, G. P. Beyer, K. Maex, A. Vantomme, M. M. Viitanen, H. H. Brongersma, et al., "Growth mechanism and continuity of atomic layer deposited TiN films on thermal SiO_2," *Journal of Applied Physics*, vol. 92, no. 12, pp. 7641- 7646, 2002.

[19] L. I. Petrova, A. A. Malkov, A. A. Malygin, and Z. P. Khim, *Russian Journal of Applied Chemistry*, vol. 64, pp. 1435, 1991.

[20] R. L. Puurunen, M. Lindblad, A. Root, and A. O. I. Krause, "Successive reactions of gaseous trimethyl aluminium and ammonia on porous alumina," *Physical Chemistry Chemical Physics*, vol. 3, pp. 1093-1102, 2001.

[21] R. L. Puurunen, "Growth per cycle in atomic layer deposition: real application examples of a theoretical model," *Chemical Vapor Deposition*, vol. 9, no. 3, pp. 327-332, 2003.

[22] M. Ritala, M. Leskela, E. Rauhala, and P. Haussalo, "Atomic layer epitaxy growth of TiN thin films," *Journal of Electrochemical Society*, vol. 142, no. 8 ,pp. 2731-2737, 1995.

[23] J. S. Becker, S. Suh, S. Wang, and R. G. Gordon, "Highly conformal thin films of tungsten nitride prepared by atomic layer deposition from a novel precursor," *Chemistry of Materials*, vol. 15, no. 15, pp. 2969-2976, 2003.

[24] A. W. Ott, J. W. Klaus, J. M. Johnson, and S. M. George, "Al_3O_3 thin film growth on Si(100) using binary reaction sequence chemistry," *Thin Solid Films*, vol. 292, no. 1-2, pp. 135-144, 1997.

[25] M. D. Groner, F. H. Fabreguette, J.W. Elam, and S. M. George, "Low temperature Al_2O_3 atomic layer deposition," *Chemistry of Materials*, vol. 16, no. 4, pp. 639-645 , 2004.

[26] R. L. Puurunen, W. Vandervorst, W. F. A. Besling, O. Richard, H. Bender, T. Conard, C. Zhao, A. Delabie, M. Caymax, S. De Gendt, et al., "Island growth in the atomic layer deposition of zirconium oxide and aluminium oxide on hydrogen-terminated silicon: Growth mode modeling and transmission electron microscopy," *Journal of Applied physics*, vol. 96, no. 9, pp. 4878-4889, 2004.

[27] H. Luth, *Surfaces and Interfaces of Solids* (Springer-Verlag, Berlin, 1993), 2nd ed.

[28] N. V. Dolgushev, A. A. Malkov, A. A. Malygin, S. A. Suvorov, A. V. Shchukarev, A. V. Beljaev, and V. A. Bykov, "Synthesis and characterization of nanosized titanium oxide films on the (0001) α-Al_2O_3 surface," *Thin Solid Films*, vol. 293, no. 1-2, pp. 91-95, 1997.

[29] L. I. Chernaya, P. E. Matkovskii, V. M. Rudakov, Y. M. Shul'ga, I. V. Markov, V. I. Tomilo, and Z. G. Bushe, *Russian Journal of General Chemistry*, vol. 62, pp. 28, 1992.

[30] R. L. Puurunen, "Random deposition as a growth mode in atomic layer deposition," *Chemical Vapor Deposition*, vol. 10, no. 3, pp. 159-170, 2004.

[31] H. Luth, *Surfaces and Interfaces of Solids* (Springer-Verlag, Berlin, 1993), 2nd ed.

[32] R. L. Puurunen, W. Vandervorst, W. F. A. Besling, O. Richard, H. Bender, T. Conard, C. Zhao, A. Delabie, M. Caymax, and S. De Gendt et al., "Island growth in the atomic layer deposition of zirconium oxide and aluminium oxide on hydrogen-terminated silicon: Growth mode modeling and transmission electron microscopy," *Journal of Applied Physics*, vol. 96, no. 9, pp. 4878-4889, 2004.

[33] R. L. Puurunen and W. Vandervorst, "Island growth as a growth mode in atomic layer deposition: a phenomenological model," *Journal of Applied Physics*, vol. 96, no. 12, pp. 7686-7695, 2004.
[34] A. Kytokivi, J. P. Jacobs, A. Hakuli, J. Merilainen, and H. H. Brongersma, "Surface characteristics and activity of chromia/alumina catalysts prepared by atomic layer epitaxy," *Journal of Catalysis*, vol. 162, no. 2, pp. 190-197, 1996.

[35] M. de Ridder, P. C. vandeven, R. G. van Welzenis, H. H. Brongersma, S. Helfensteyn, C. Creemers, P. Van Der Voort, M. Baltes, M. Mathieu, and E. F. Vansant, "Growth of iron oxide on yittria-stabilized zirconia by atomic layer deposition," *Journal of Physical Chemistry B*, vol. 106, no. 51, pp. 13146-13153, 2002.

[36] J. Becker, "Atomic Layer Deposition of Metal Oxide and Nitride Thin Films," Ph.D. dissertation, Department of Chemistry and Chemical Biology, Cambridge, Massachusetts.

[37] M. Ritala and M. Leskela, " *Handbook of Thin Film Materials*," Academic Press, pp.113, 2002.

[38] M. Ylilammi, "Monolayer thickness in atomic layer deposition," *Thin Solid Films*, vol. 279, no. 1-2, pp- 124-130, 1996.

[39] R.L. Puurunen, "Growth per cycle in atomic layer deposition: a theoretical model," *Chemical Vapor Deposition*, vol. 9, no. 5, pp. 249-257, 2003.

[40] S. Heil, "Plasma-Assisted Atomic Layer Deposition of Metal Oxides and Nitrides," Ph.D. dissertation, Technische Universiteit Eindhoven, 2007.

[41] C. Ozgit-Akgun, E. Goldenberg, A. K. Okyay, and N. Biyikli, "Hollow cathode plasma-assisted atomic layer deposition of crystalline AlN, GaN and $Al_xGa_{1-x}N$ thin films at low temperatures," *Journal of Material Chemistry* C, vol. 2, no. 12, pp. 2123-2136, 2014.

[42] K. Watanabe, T. Taniguchi, and H. Kanda, "Direct-bandgap properties and evidence for ultraviolet lasing of hexagonal boron ntride single crystal," *Nature Materials*, vol. 3, no. 6, pp. 406-409, 2004.

[43] C. R. Dean, A. F. Young, I. Meric, C. Lee, L. Wang, S. Sorgenfrei, K. Watanabe , "Boron nitride substrates for high-quality graphene electronics," *Nature Nanotechnology*, vol. 5, no. 10, pp. 722-726, 2010.

[44] R. T. Paine and C. K. Narula, "Synthetic routes to boron nitride," *Chemical reviews*, vol. 90, no. 1, pp. 73-91, 1990.

[45] K. Watanabe, T. Taniguchi, T. Niiyama, K. Miya, and M. Taniguchi, "Far-ultraviolet plane-emission handheld device based on hexagonal boron nitride," *Nature Photonics*, vol. 3, no. 10, pp. 591-594, 2009.

[46] Y. Kubota, K. Watanabe, O. Tsuda, and T. Taniguchi, "Deep ultraviolet light–emitting hexagonal boron nitride synthesized at atmospheric pressure," *Science*, vol. 317, no. 5840, pp. 932-934, 2007.

[47] R. W. Trice and J. W. Halloran, "Elevated-temperature mechanical properties of silicon nitride/boron nitride fibrous monolithic ceramics," Journal *of American Ceramic Society*, vol. 83, no. 2, pp. 311-316, 2000.

[48] R. W. Trice and J. W. Halloran, "Investigation of the physical and mechanical properties of hot-Pressed boron nitride/oxide ceramic composites," *Journal of American Ceramic Society*, vol. 82, no. 9, pp. 2563-2565, 1999.

[49] D. H. Choa, J. S. Kima, S. H. Kwona, C. Lee, and Y. Z. Lee, "Evaluation of hexagonal boron nitride nano-sheets as a lubricant additive in water" *Wear*, vol. 302, no. 1-2, pp. 981, 2013.

[50] D. J. Kester and R .Messier, "Phase control of cubic boron nitride thin films," *Journal of Applied Physics*, vol. 72, no. 2, pp. 504-513, 1992.

[51] M. Goto, A. Kasahara, M. Tosa, T. Kimura, and K. Yoshihara, "characteristics of thin films of hexagonal boron nitride mixed with copper controlled by a magnetron co-sputtering deposition technique," *Applied Surface science*, vol. 185, no. 3-4, pp. 172-176, 2002.

[52] P. C. Huang and M. S. Wong, "nanostructures of mixed-phase boron nitride via biased microwave plasma-assisted CVD," *Vaccum*, vol. 100, pp. 66-70, 2014.

[53] W. A. Yarbrough, "Current research problems and opportunities in the vapor phase synthesis of diamond and cubic boron nitride," *Journal of Vaccum Science and Ttechnology*, vol. 9, no. 3, pp. 1145-1152, 1991.

[54] A. Bartl, S. Bohr, R. Haubner, and B. Lux, "A comparison of low-pressure CVD synthesis of diamond and c-BN," *International Journal of Refractory Materials*, vol. 14, no. 1-3, pp. 145-157, 1996.

[55] H. O. Pierson, "Boron nitride composites by chemical vapor deposition," *Journal of Composite Materials*, vol. 9, no. 3, pp. 228, 1975.

[56] A. S. Rozenberg, Yu. A. Sinenko, and N. V. Chukanov, "Regularities of pyrolytic boron nitride coating formation on a graphite matrix," *Journal of Material Science*, vol. 28, no. 20, pp. 5528-5533, 1993.

[57] S. Middleman, "The Role of gas-phase reactions in boron nitride growth by chemical vapor deposition," *Materials Science and Engineering: A*, vol. 163, no. 1, pp. 135-140, 1993.

[58] B. Marlid, M. Ottosson, U Pettersson, K. Larsson, and J. Otto. Carlsson, "Atomic layer deposition of BN thin films," *Thin Solid Films*, vol. 402, no. 1-2, pp. 167-171, 2002.

[59] J. D. Ferguson, A. W. Weimer, and S. M. George, "Atomic layer deposition of boron nitride using sequential exposures of BCl_3 and NH_3," *Thin Solid Films*, vol. 413, no. 1-2, pp. 16-25, 2002.

[60] J. Olander, L. M. Ottosson, P. Heszler, J. O. Carlsson, and K. M. E. Larsson, "Laser assisted atomic layer deposition of boron nitride thin film," *Chemical Vapor Deposition*, vol. 11, no. 6-7, pp. 330-337, 2005.

[61] J. L. Huang, C. H. Pan, and D. F. Lii, "Investigation of the BNc films prepared by low pressure chemical vapor deposition," *Surface Coating Technology*, vol. 122, no. 2-3, pp. 166-175, 1999.

[62] F. Rebillat, A. Guette, and C. R. Brosse, "Chemical and mechanical alterations of SiC nicalon fibers properties during the CVD/CVI process for boron nitride," *Acta Materialia*, vol. 47, no. 5, pp. 1685-1696, 1999.

[63] W. Auwarter, T. J. Kreutz, T. Greber , and J. Osterwalder, "XPD and STM investigation of hexagonal boron nitride on Ni(111)," *Surface Science*, vol. 429, no. 1-3, pp. 229-236, 1999.

[64] P. Sutter, J. Lahiri, P. Albrecht, and E. Sutter, "Chemical vapor deposition and etching of high quality monolayer hexagonal boron nitride films," *ACS Nano*, vol. 5, no. 9, pp. 7303-7309, 2011.

[65] Z. Zhou, J. J. Zhao, Y. S. Chen, P. V. Schleyer, and Z. F. Chen, "Energetics and electronic structures of AlN nanotubes/wires and their potential application as ammonia sensors," *Nanotechnology*, vol. 18, no. 42, pp. 424023, 2007.

[66] A. Ahmadi, N. L. Hadipour, M. Kamfiroozi, and Z. Bagheri, "Theoretical study of aluminium nitride nanotubes for chemical sensing of formaldehyde," *Sensors and Actuatators B: Chemical*, vol. 161, no. 1, pp. 1025-1029, 2012.

[67] C. Ozgit-Akgun, F. Kayaci, I. Donmez, T. Uyar, and N. Biyikli, "Template-based synthesis of aluminium nitride hollow nanofibers via plasma-enhanced

atomic layer deposition" *Journal of American Ceramic Society*, vol. 96, no. 3, pp. 916-922, 2013.

[68] R. T. Paine and C. K. Narula, "Synthetic routes to boron nitride," *Chemical Reviews*, vol. 90, no. 1, pp. 73-91, 1990.

[69] D. Golberg, Y. Bando, C. C. Tang, and C. Y. Zhi, "Boron nitride nanotubes," *Advance Materials*, vol. 19, no. 18, pp. 2413-2432, 2007.

[70] N. G. Chopra, R. J. Luyken, K. Cherrey, V. H. Crespi, M. L. Cohen, S. G. Louie, A. Zettl, "Boron-nitride nanotubes," *Science*, vol. 269, no. 5226, pp. 966-967, 1995.

[71] A. Loiseau, F. Willaime, N. Demoncy, G. Hug, H. Pascard, "Boron nitride nanotubes with reduced numbers of layers synthesized by arc discharge," *Physical Review Letters*, vol. 76, no. 25, pp. 4737-4740, 1996.

[72] M. Terrones, W. K. Hsu, H. Terrones, J. P. Zhang, S. Ramos, J. P. Hare, R. Castillo, K. Prassides, A. K. Cheetham, H. W. Kroto, D. R. M. Walton, "Metal particle catalysed production of nanoscale BN structures," *Chemical Physics Letters*, vol. 259, no. 5-6, pp. 568-573, 1996.

[73] D. Golberg, Y. Bando, M. Eremets, K. Takemura, K. Kurashima, H. Yusa, "Nanotubes in boron nitride laser heated at high pressure," *Applied Physics Letters*, vol. 69, no. 14, pp. 2045-2047, 1996.

[74] O. R. Lourie, C. R. Jones, B. M. Bartlett, P. C. Gibbons, R. S. Ruoff, W. E. Buhro, "CVD growth of boron nitride nanotubes," *Chemistry of Materials*, vol. 12, no. 7, pp. 1808-1810, 2000.

[75] W. Zhou, Z. L. Wang, *Scanning Microscopy for Nanotechnology, Techniques and Applications*, ISBN: 978-0-387-33325-0

[76] G. Binnig, C. F. Quate, and C. H. Gerber, "Atomic Force Microscope," Physical Review Letters, vol. 56, no. 9, pp. 930-934, 1996.

[77] C. D wagner, W. M. Riggs, L. E Davis, J. F Moulder, and G. E. Muilenberg, *Handbook of X-ray photoelectron spectroscopy*, Perkin Elmer Corporation Minnesota, December 1978

[78] From the website: http://www.chem.qmul.ac.uk/surfaces/scc/scat5_3.htm

[79] From the website: http://www.panalytical.com/index.cfm?pid=314

[80] From the website: http://web.pdx.edu/~pmoeck/phy381/Topic5a-XRD.pdf

[81] From the website: http:/www.chem.sc.edu/faculty/zurloye/xrdtutorial_ 2013.pdf

[82] From the website: http://www.matter.org.uk/tem/

[83] E. Rosencher, *Optoelectronics*; pp. 304. Cambridge university press, Newyork, 2002.

[84] M. Ylilammi, "Monolayer thickness in atomic layer deposition," *Thin Solid Films*, vol. 279, no. 1-2, pp. 124-130, 1996.

[85] R. L. Puurunen, "Growth per cycle in atomic layer deposition: a theorethical model," *Chemical Vapor Deposition*, vol. 9, no. 5, pp. 249-257, 2003.

[86] A. W. Ott, J. W. Klaus, J. M. Johnson, and S. M. George, " Al_3O_3 thin film growth on Si(100) using binary reaction sequence chemistry," *Thin Solid Films*, vol. 292, no. 1-2, pp. 135-144, 1997.

[87] M. Putkonen, M. Nieminen, and L. Niinisto, "Magnesium aluminate thin films by atomic layer deposition from organometallic precursors and water," *Thin Solid Films*, vol. 466, no. 1-2, pp. 103-107, 2004.

[88] W. Auwarter, T. J. Kreutz, T. Greber , and J. Osterwalder, "XPD and STM investigation of hexagonal boron nitride on Ni(111)," *Surface Science*, vol. 429, no. 1-3, pp. 229-236, 1999.

[89] P. Sutter, J. Lahiri, P. Albrecht, and E. Sutter, "Chemical vapor deposition and etching of high quality monolayer hexagonal boron nitride Films," *ACS Nano*, vol. 5, no. 9, pp. 7303-7309, 2011.

[90] M. Belyansky, M. Trenary, and C. Ellison, "Boron chemical shifts in B_6O," *Surface science spectra*, vol. 3, no. 2, pp. 147-150, 1994.

[91] D. N. Hendrickson, J. M. Hollander, and W. L. Jolly, "Core-electron binding energies for compounds of boron, carbon, and chromium," *Inorganic Chemistry*, vol. 9, no. 3, pp. 612-615, 1970.

[92] Z. F. Song, S. Z. Ye, Z. Y. Chen, L. Song, and J. Shen, "Study on boron-film thermal neutron converter prepared by pulsed laser deposition," *Applied Radiation Isotopes*, vol. 69, no. 2, pp. 443-447, 2011.

[93] L. G. Jacobsohn, R. K. Schulze, M. E. H. Maia da Costa, and M. Nastasi, "X-ray photoelectron spectroscopy investigation of boron carbide films deposited by sputtering," *Surface Science*, vol. 572, no. 2-3, pp. 418-424, 2004.

[94] M. Das, A. K. Basua, S. Ghataka, and A. G. Joshib, "Carbothermal synthesis of boron nitride coating on PAN Carbon Fiber," *Journal of Euorpean Ceramic Society*, vol. 29, no. 10, pp. 2129-2134, 2009.

[95] M. A. Mannan, M. Nagano, K. Shigezumi, T. Kida, N. Hirao, and Y. Baba, "Characterization of boron carbonitride (BCN) thin films deposited by radiofrequency and microwave plasma enhanced chemical vapor deposition," *American Journal of Applied Science*, vol. 5, no. 6, pp. 736-741, 2007

[96] X. Gouin, P. Grange, L. Bois, P. L'Haridon, and Y. Laurent, Characterization process of the nitridation process of boric acid," *Journal of Alloys and Compounds*, vol. 224, no. 1, pp. 22-28, 1995.

[97] T. Thamm, D. Wett, W. Bohne, E. Strub, J. Rohrich, R. Szargan, G. Marx, and W. A. Goedel, "Investigations on PECVD boron barbonitride layers by means of ERDA, XPS and nano-indentation measurements," *Microchimica Acta*, vol. 156, no. 1-2, pp. 53-56, 2007.

[98] A. Pakdel, Y. Bando, D. Shtansky, and D. Golberg, "Non wetting and optical properties of BN nanosheet films," *Surface Innovations*, vol. 1, no. 1, pp. 32-39, 2012.

[99] D. M. Hoffman, G. L. Doll, and P. C. Eklund, "Optical properties of pyrolytic boron nitride in the energy range 0.05-10 eV," *Physical Reviews B*, vol. 30, no. 10, pp. 6051-6056, 1984.

[100] V. L. Solozhenko, A. G. Lazarenko, J. P. Petitet, and A. V. Kanaev, "Bandgap energy of graphite-like hexagonal boron nitride," *Journal of Physics and Chemistry of Solids*, vol. 62, no. 7, pp. 1331-1334, 2001.

[101] L. Museur, E. Feldbach, and A. Kanaev, "Defect-related photoluminescence of hexagonal boron nitride," *Physical Reviews B*, vol. 78, no. 15, pp. 1552041-1552048, 2008.

[102] A. Abdellaoui, A. Bath, B. Bouchikhi, and O. Baehr, "Structure and optical properties of boron nitride thin films prepared by PECVD," *Material Science Engineering B*, vol. 47, no. 3, pp. 257-262, 1997.

[103] T. A. Anutgan, M. Anutgan, I. Atilgan, and B. Katircioglu, "Stability and degradation of plasma deposited boron nitride thin films in ambient atmosphere," *Thin Solid Films*, vol. 518, no. 1, pp. 419-425, 2009.

[104] C. Guimon, D. Gonbeau, G. Pfister-Guillouzo, O. Dugne, A. Guette, R. Naslain and M. Lahaye, "XPS study of BN thin films deposited by CVD on SiC plane substrates," *Surface and Interface Analysis*, vol. 16, no. 1-12, pp. 440-445,1990.

[105] R. K. Brow, "An XPS study of oxygen bonding in zinc phosphate and zinc borophosphate glasses," *Journal of Non-Crystalline Solids*, vol. 194, no. 3, pp. 267-273, 1996.

[106] W. J. Gammon, O. Kraft, A. C. Reilly, B. C. Holloway, "Experimental comparison of N(1s) X-ray photoelectron spectroscopy binding energies of hard and elastic amorphous carbon nitride films with reference organic compounds," *Carbon*, vol. 41, no. 10, pp. 1917-1923, 2003.